Monthly Notices
of the
ROYAL ASTRONOMICAL SOCIETY

MNRAS **523,** 4720–4738 (2023) https://doi.org/10.1093/mnras/stad1698
Advance Access publication 2023 June 8

The 3D kinematics of stellar substructures in the periphery of the Large Magellanic Cloud

Camila Navarrete,[1,2★†] David S. Aguado,[3,4,5★] Vasily Belokurov,[6,7] Denis Erkal,[8] Alis Deason,[9,10] Lara Cullinane[11] and Julio Carballo-Bello[12†]

[1] *ESO – European Southern Observatory, Alonso de Cordova 3107, Vitacura, Santiago, Chile*
[2] *Université Côte d'Azur, Observatoire de la Côte d'Azur, CNRS, Laboratoire Lagrange, Bd de l'Observatoire, CS 34229, F-06304 Nice cedex 4, France*
[3] *Instituto de Astrofísica de Canarias, Vía Láctea, E-38205 La Laguna, Tenerife, Spain*
[4] *Departamento de Astrofísica, Universidad de La Laguna, E-38206 La Laguna, Tenerife, Spain*
[5] *Dipartimento di Fisica e Astrofisica, Univerisità degli Studi di Firenze, via G. Sansone 1, I-50019 Sesto Fiorentino, Italy*
[6] *Institute of Astronomy, University of Cambridge, Madingley Road, Cambridge CB3 0HA, UK*
[7] *Center for Computational Astrophysics, Flatiron Institute, 162 5th Avenue, New York, NY 10010, USA*
[8] *Department of Physics, University of Surrey, Guildford GU2 7XH, UK*
[9] *Institute for Computational Cosmology, Department of Physics, Durham University, South Road, Durham DH1 3LE, UK*
[10] *Centre for Extragalactic Astronomy, Department of Physics, Durham University, South Road, Durham DH1 3LE, UK*
[11] *Department of Physics and Astronomy, Johns Hopkins University, Baltimore, MD 21218, USA*
[12] *Instituto de Alta Investigación, Universidad de Tarapacá, Casilla 7D, 1001236 Arica, Chile*

Accepted 2023 June 5. Received 2023 April 27; in original form 2023 February 8

ABSTRACT

We report the 3D kinematics of 27 Mira-like stars in the northern, eastern, and southern periphery of the Large Magellanic Cloud (LMC), based on *Gaia* proper motions and a dedicated spectroscopic follow-up. Low-resolution spectra were obtained for more than 40 Mira-like candidates, selected to trace known substructures in the LMC periphery. Radial velocities and stellar parameters were derived for all stars. *Gaia* data release 3 astrometry and photometry were used to discard outliers, derive periods for those stars with available light curves, and determine their photometric chemical types. The 3D motion of the stars in the reference frame of the LMC revealed that most of the stars, in all directions, have velocities consistent with being part of the LMC disc population, out of equilibrium in the radial and vertical directions. A suite of numerical simulations was used to constrain the most likely past interaction history between the Clouds given the phase-space distribution of our targets. Model realizations in which the Small Magellanic Cloud (SMC) had three pericentric passages around the LMC best resemble the observations. The interaction history of those model realizations has a recent SMC pericentric passage (∼320 Myr ago), preceded by an SMC crossing of the LMC disc at ∼0.97 Gyr ago, having a radial crossing distance of only ∼4.5 kpc. The previous disc crossing of the SMC was found to occur at ∼1.78 Gyr ago, with a similar radial crossing distance of ∼5.6 kpc.

Key words: galaxies: interactions – galaxies: kinematics and dynamics – Magellanic Clouds – galaxies: structure.

1 INTRODUCTION

The Magellanic Family is the poster child for binary dwarf galaxy collisions. Thanks to the advanced stage and overt intensity of the Clouds' interaction, we have a rare opportunity to directly observe a variety of phenomena normally postulated to accompany and induce galaxy transformations. This includes tidal stripping and torquing, ram pressure gas removal, dynamical friction, and merger-induced star formation.

Several pieces of evidence in their morphologies reflect the intense past interaction history of this system. For example, the Large Magellanic Cloud (LMC) off-set stellar bar (Zhao & Evans 2000; Choi et al. 2018) and associated spiral arms (see Grady, Belokurov & Evans 2021), truncation of its outer stellar disc (Mackey et al. 2018) evident in both Red Giants and RR Lyrae (Grady et al. 2021), and the presence of warps (Olsen & Salyk 2002; Choi et al. 2018). The past orbit of the Clouds suggests that they have experienced a recent close pericentric passage ≤250 Myr ago, consistent with the expected formation time of the Magellanic Bridge (Choi et al. 2018). Besides this 'direct' collision (impact parameter of ≲ 10 kpc), the details of previous interactions are not yet fully constrained.

In the periphery of the LMC, numerous stellar substructures – in the form of arms, clumps, streams and bridges – have been found thanks to wide-field deep-photometric surveys, as well as astrometric data from the *Gaia* mission. This plethora of substructures reflects its complex interaction history with the Small Magellanic Cloud

---

★ E-mail: camila.navarrete@oca.eu (CN); david.aguado@iac.es (DSA)
† Visiting astronomer, Cerro Tololo Inter-American Observatory, NSF's NOIRLab, which is managed by the Association of Universities for Research in Astronomy (AURA) under a cooperative agreement with the National Science Foundation.

Published by Oxford University Press on behalf of Royal Astronomical Society

(SMC) and/or the Milky Way. Towards the north, a thin and long stellar stream was first presented in Mackey et al. (2016), being subsequently studied in detail by several studies (e.g. Belokurov & Erkal 2019; El Youssoufi et al. 2021; Gaia Collaboration 2021; Cullinane et al. 2022a). Towards the east, a diffuse and extended stellar overdensity has been recovered based on different stellar tracers, receiving a variety of names (e.g. ‘Eastern Substructure 1’, ‘Eastern Substructure 2’; El Youssoufi et al. 2021). A large, broad and diffuse substructure in the Southern vicinity of the LMC, known as the old bridge (Belokurov et al. 2017), has been resolved into thin stellar streams (Mackey et al. 2018; Belokurov & Erkal 2019; El Youssoufi et al. 2021). The origin of these different stellar substructures around the Clouds is not yet established, although most of them are thought to be part of the disturbed outer LMC disc based on the properties of their stellar populations and in-plane velocities.

Radial velocities, and with them, full 6D phase-space information for the stars in these substructures, is of paramount importance to understand their motions and assess their possible origin. To date, a limited number of works have collected spectroscopic information for this purpose. In Cullinane et al. (2020), the *Magellanic Edge Survey (MagES)* is described, which collects multi-object spectroscopy of red giant branch and red clump stars. The *MagES* survey has analysed the northern arm (Cullinane et al. 2020), the outer LMC stellar population (Cullinane et al. 2022b), and the SMC outskirts (Cullinane et al. 2023). Similarly, in Cheng et al. (2022), the results from APOGEE-2 observations in six fields towards the north and south of the LMC were presented.

While these previous observations were based on red giant branch and/or red clump stars, the errors on the proper motions of these stars tend to be larger than for the most luminous tracers. Moreover, at fields at larger distances from the LMC centre, contamination from Milky Way foreground stars can be non-negligible (Jiménez-Arranz et al. 2023). More luminous and less abundant tracers are thus well-suited to uncover the diffuse substructures in the LMC outskirts, as their contamination rate is smaller. Particularly, Deason et al. (2017) recovered several of the well-known stellar substructures around the LMC based on candidate Mira stars. Being ≈ 3.5 mag brighter than Red Clump stars, these require only moderate exposure times to derive reliable radial velocities. Motivated by this, we carried out a spectroscopic follow-up of more than 40 Mira-like stars in the vicinity of the Clouds, aiming to recover their phase-space information and use them to constrain the past interaction history of the Clouds.

This paper is organized as follows: in Section 2, a summary of the target selection for the spectroscopic follow-up is described. In Section 3, observations and data reduction are discussed. In Section 4, we present the spectroscopic analysis of our sample. Additional parameters such as parallax, periods, and heliocentric distances are discussed in Section 5. 3D cylindrical velocities in the LMC reference frame for the stars in the immediate LMC periphery are derived in Section 6. Finally, Section 7 presents a comparison between the observations and numerical simulations, while Section 8 presents the summary and conclusions of this work.

2 TARGET SELECTION

Candidate Mira variable stars were selected from *Gaia* DR1 data following the procedure outlined in Deason et al. (2017). In that work, repeated observations of sources during the initial phase of the *Gaia* mission were used to identify stars that show signs of variability. In particular, the *Gaia* ‘variability amplitude’ was used: $A = \sqrt{N_{\rm obs}}\sigma(F)/F$, where, $N_{\rm obs}$ is the number of CCD crossings, and F and $\sigma(F)$ are the flux and flux error, respectively (see also Belokurov et al. 2017). This variability information was combined with infrared photometry from the Two Micron All Sky Survey (2MASS; Skrutskie et al. 2006) and the *Wide-field Infrared Survey Explorer* (*WISE*; Wright et al. 2010) to select candidate giant stars in the vicinity of the LMC. For more details, please see section 2 of Deason et al. (2017).

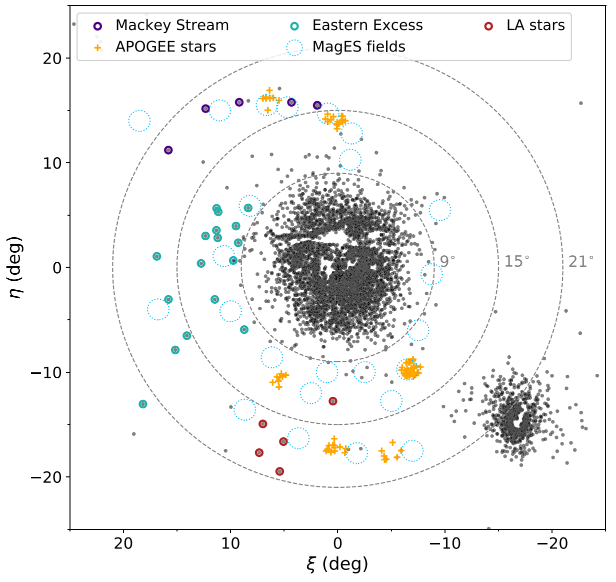

Figure 1. Mira candidates in the vicinity of the LMC and SMC, selected following the cuts detailed in Deason et al. (2017). The coordinates (ξ, η) are in the gnomonic (tangent-plane) projection. The dashed circles correspond to 9°, 15°, and 21° of angular separation from the LMC centre. The targets selected for follow-up observations are marked with coloured circles, including five stars in the so-called Mackey Stream, 17 stars from the Eastern excess group, and five stars in the LA group. Blue unfilled circles mark the position of the fields in Cullinane et al. (2022b) while yellow crosses are individual stars analysed in Cheng et al. (2022).

We select a subsample of these giant candidates for low-resolution spectroscopic follow-up to derive radial velocities and metallicities. In particular, we focus on the periphery of the Clouds, where there are interesting groups of stars to the East (‘Eastern excess’, EE), North (‘Mackey Stream’, MS), and South (possibly associated with the Leading Arm, dubbed ‘LA’) of the LMC. Fig. 1 shows the location of the individual Mira-like stars observed, in a gnomonic (tangent-plane) projection, where the tangent point is located at the centre of the LMC $(\alpha_0,\ \delta_0) = (82\overset{\circ}{.}25,\ -69\overset{\circ}{.}5)$. All the Mira candidates from Deason et al. (2017) are shown as grey points. The locations of two previous spectroscopic campaigns around the periphery of the Clouds are included for reference (fields from Cullinane et al. 2022a and stars from Cheng et al. 2022). We also targeted some candidate giants away from the Magellanic Clouds (BP), which are above the disc plane (see Fig. 2). These could potentially be associated with Magellanic debris or distant halo stars with a different origin (see Section 5.4.2 for further discussion).

3 OBSERVATIONS AND DATA REDUCTION

Mira candidates in the Magellanic periphery were observed for 4 nights with the COSMOS spectrograph (Martini et al. 2014) on the 4m Víctor Blanco telescope at Cerro Tololo Inter-American

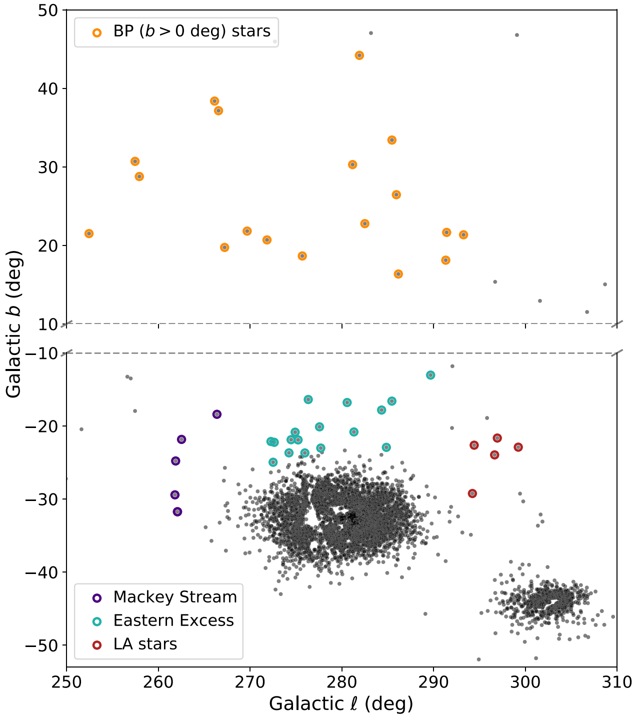

Figure 2. Galactic coordinate distribution of our target Mira-like stars. The three groups in the vicinity of the LMC and SMC (‘Mackey Stream’, ‘Eastern excess’, and ‘LA’) are the same targets as shown in Fig. 1. The 17 target stars above the Galactic plane (‘BP’ group) are shown as orange open circles.

Observatory (CTIO).[1] Long-slit spectra for 45 Mira candidate stars were obtained using the Blue VPH Grism covering a wavelength range of 5600–9600 Å and a 1.0 arcsec slit, reaching a spectral resolution of ∼2000. Single exposures of 300s to 1800s per target were acquired, as well as one or two wavelength calibration arcs with Hg + Ne lamps observed at the same airmass as the targets. Radial velocity standard Miras (R Lep, HD 75021; Menzies, Feast & Whitelock 2006) were also observed each night, with exposure times of 0.5 to 5 s.

A standard data reduction (flat-fielding, bias subtraction, extraction, and wavelength calibration) was performed with the *onespec* package in IRAF.[2] (Tody 1993). The lamps used were the non-standard Hg + Ne more suitable for calibration in the red part of the spectrum. A barycentric correction is then performed for each individual exposure, considering the Julian date, the place of the observatory on the surface of the Earth and the coordinates of each object.

4 SPECTROSCOPIC ANALYSIS

The spectra of Mira variables change significantly during their pulsation cycle; therefore stellar parameters (brightness, opacity, and surface temperature) are phase dependant. In addition, shock waves in the pulsating atmospheres of Mira variables can produce emission lines. In particular, close to the maximum brightness, they show very strong H α emission lines (Joy 1926). Several objects in our sample (13 out of 45) show these emission lines (see Fig. 3).

4.1 Radial velocity estimates

To derive radial velocities ($V_{\rm rad}$), we first corrected the spectra for barycentric motion calculated with the `rvcorrect` package. We then used `fxcor` to calculate the cross-correlation function (CCF) based on the algorithm by Tonry & Davis (1979), using a template computed with the ASSϵT code (Koesterke, Allende Prieto & Lambert 2008) by assuming the following stellar parameters: $T_{\rm eff}$ = 4000 K, log g = 1, and [Fe/H] = –1.0.

Under our observational setup, the COSMOS data cover a region severely affected by telluric absorption. We therefore employed the region around the Ca II triplet (8498, 8542, and 8662 Å) for cross-correlation assuming the stellar Calcium origin. Depending on the quality of the Ca triplet, we derived a range of V$_{\rm rad}$ uncertainties up to 80 km s^{-1} but the average value is ∼15 km s^{-1}. The derived radial velocities and uncertainties are summarized in Table 1.

We also measured the $V_{\rm rad}$ difference with emission lines (H α) when available; the results were in agreement with Menzies et al. (2006) with reported shifts up to 30 km s^{-1} along the pulsating phase. Our derived values are shown in Table 1. Furthermore, we do not observe Ca in emission in contrast with Gillet et al. (1985) that reported both 8498 and 8542 Å lines in emission for several stars, suggesting our observations were not made close to the maximum of the pulsation cycle.

At the time of our observations, only *Gaia* DR1 was available, without any measurement of radial velocities. Presently, the *Gaia* DR3 (Gaia Collaboration 2023) main source catalogue contains radial velocity measurements for more than 33 million sources with magnitudes $G_{\rm RVS}$ < 14 mag. Table 2 presents the radial velocities reported in the *Gaia* DR3 main source catalogue, after cross-matching with our target stars, using a 1.0 arcsec matching radius. 26 out of the 45 stars observed with COSMOS have radial velocities reported in *Gaia*. There is an overall good agreement between those values and the ones derived based on the COSMOS spectra (see Fig. 4). This agreement reinforces our assumption that the possible radial velocity variations due to the pulsation cycle are of the order of magnitude of the measured uncertainties. Given their relatively faint magnitudes, Gaia radial velocities for our targets were obtained from the maximum of the averaged cross-correlation function of the individual measurements (see Katz et al. 2023), and the individual radial velocity measurements and their respective date and time of observations are not part of the Gaia DR3. Therefore, it is not possible to verify if the differences in radial velocities measured by Gaia and those based on the COSMOS data are due to the observations being obtained at different pulsation phases.

Two of our targets, EE10 and EE14, have been observed by the APOGEE-S survey (Santana et al. 2021), as part of one of the contributed programmes.[3] The reported averaged heliocentric velocity for EE10 ($V_{\rm helio}$ = 299.008 km s^{-1}) is in good agreement with the value derived in this work. The APOGEE and COSMOS observations were obtained at similar phases during the pulsation cycle (0.28 and 0.30, respectively, based on the period reported in Table 3), consistent with a small difference in the measured velocities. In the case of EE14, the APOGEE heliocentric velocity, $V_{\rm helio}$ = 325.624 km s^{-1}, is ∼65 km s^{-1} larger than the value measured in this work, although this star has one of the largest

---

[1] Chilean time proposal CN2017B-0910.

[2] IRAF is distributed by the National Optical Astronomy Observatory, which is operated by the Association of Universities for Research in Astronomy (AURA) under cooperative agreement with the National Science Foundation.

[3] `PROGRAMNAME` = ‘TeskeVanSaders_18a’.

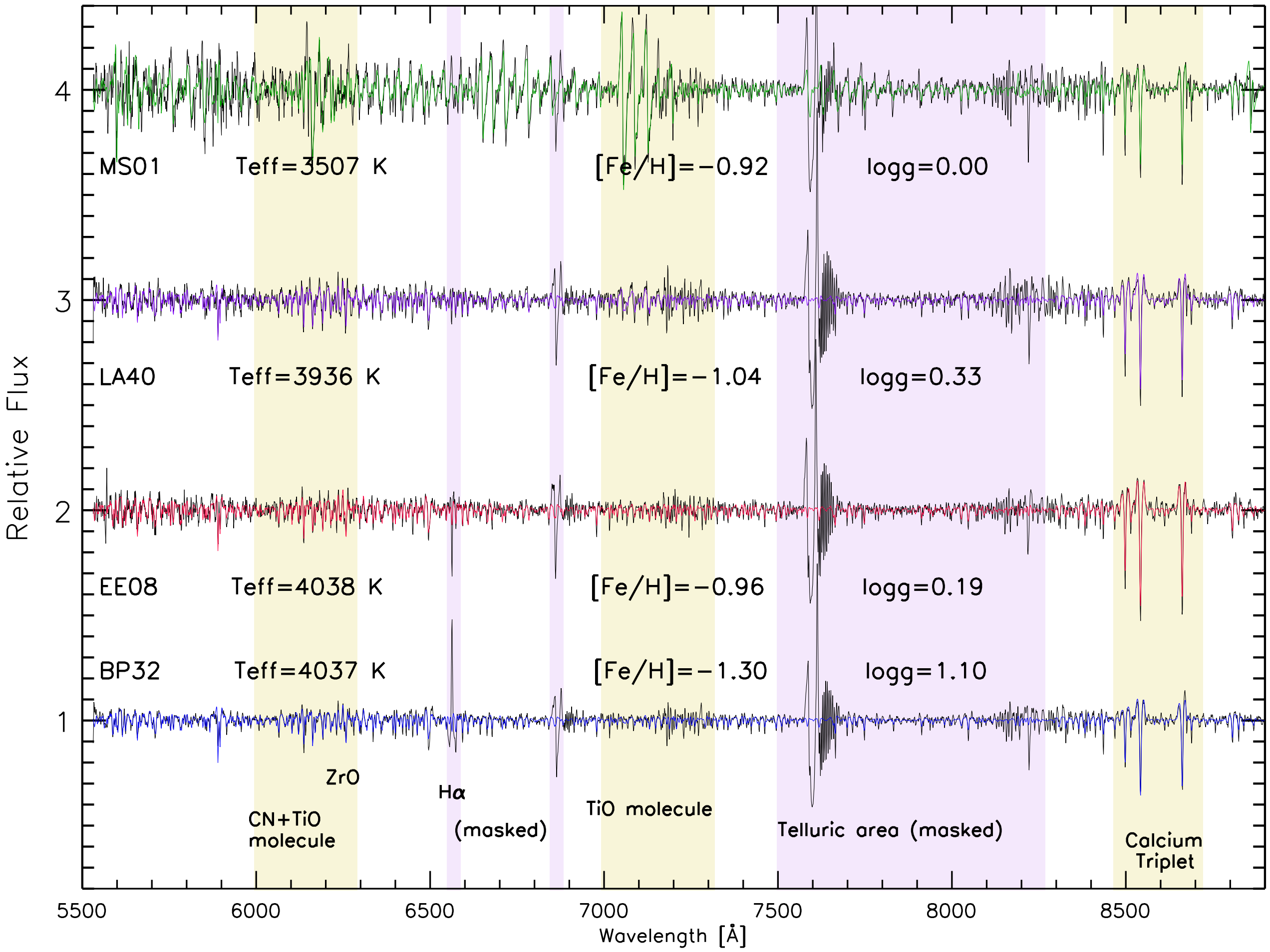

Figure 3. COSMOS spectra for a subsample of the observed targets together with the best fit derived with FERRE. The main stellar parameters derived for each target are also displayed. Yellow shadowed regions are relevant regions (e.g. location of the Calcium triplet), while purple shadowed areas are those masked and not used for the FERRE fit.

radial velocity errors (~ 80 km s^{-1}). Moreover, the velocities were obtained at different phases (0.27 for APOGEE, 0.03 for COSMOS spectra), which can contribute to such different velocities.

As almost 20 of our targets do not have radial velocities reported in *Gaia*, and those stars that have measurements available (from Gaia and/or APOGEE) are in good agreement with our measurements, the following analysis will use the COSMOS radial velocities.

4.2 Stellar parameters

Assuming possible slight variations as a function of the pulsation phase, we derive stellar parameters by spectroscopic fitting with the FERRE code[4] (Allende Prieto et al. 2006). FERRE is able to employ different algorithms to minimize the χ^2 against a library of stellar spectra (Allende Prieto et al. 2018). Then, by interpolating within the nodes of the grid, the code provides the best stellar model and the most likely effective temperature ($T_{\rm eff}$), surface gravity ($\log g$) and overall metallicity ([Fe/H]).

Both the data and the models were normalized with a running mean filter of 30 pixels. For the purpose of spectroscopic analysis, we masked the Balmer-α line and the regions most affected by telluric lines. Thus, the code does not take into consideration the χ^2 from those areas. In Fig. 3, we show a subsample of four spectra and the best fit derived with FERRE. Relevant areas are shaded in yellow while the masked regions are coloured in purple.

In Table 1, we also provide a quality flag by visual inspection of each FERRE fit. In some cases, due to the relatively low quality of the spectra and/or the presence of significant telluric lines, even outside of our masked area, it was not possible to obtain a good fit. For these cases, we set `flag = 0`; for the remainder we set `flag = 1`. Additionally, we performed a complementary analysis deriving metallicities for the entire sample by only considering the information contained in the region of the Calcium triplet around 8400–8700 Å. We fixed $T_{\rm eff}$ and $\log g$ from the FERRE analysis, and then calculated $[{\rm Fe/H}]_{\rm CaT}$ masking everything outside of the considered region. The results are summarized in Table 1, and in most cases are in good agreement with the [Fe/H]. However, in some cases, we find a significant deviation between the two determinations, up to 1 dex. The majority of these cases corresponds to objects with `flag = 0`, indicating the fit is poor. However, there are 7 cases – BP34, EE10, EE17, EE21, LA42, LA44, and MS04 – where the fit appears reasonable but the metallicities are incompatible. Those objects are quite cool ($T_{\rm eff} < 3800$ K) and the combination of strong molecular bands and the presence of telluric lines could explain the

---

[4] `FERRE` is available from http://github.com/callendeprieto/ferre.

Table 1. Mira variable candidate stars observed with the COSMOS spectrograph. Columns give the equatorial coordinates of the stars, radial velocities, and stellar parameters derived from the spectra (see Section 4). The last column gives the quality 'Flag' for the derived stellar parameters, with `flag = 0` for those spectra where the spectroscopic fitting is unreliable.

ID	R.A. (hh:mm:ss.s)	Dec (dd:mm:ss)	V_{rad} (km s^{-1})	σ_{Vrad} (km s^{-1})	H_{emi} (Å)	RV shift (km s^{-1})	[Fe/H]	T_{eff} (K)	log g (cm s^{-2})	[Fe/H]$_{\mathrm{CaT}}$	Flag
BP22	10:10:29.0	–31:44:53	320.39	6.71			–1.13	4091.71	0.68	–1.05	1
BP23	11:55:27.4	–39:57:44	158.24	9.55	6562.25	–25.04	–0.91	3939.74	0.81	–1.11	1
BP24	11:17:16.7	–36:20:11	324.31	7.60			–1.07	3834.37	0.00	–1.52	1
BP25	10:29:52.7	–33:29:26	39.59	10.69	6562.74	–2.79	–0.99	4013.93	0.49	–0.98	1
BP26	10:39:36.2	–37:08:53	109.06	9.56			–1.18	3747.15	0.00	–0.98	1
BP27	10:24:57.2	–31:25:47	313.41	10.67			–1.11	4039.59	0.38	–1.26	1
BP28	10:11:16.3	–17:41:28	156.86	43.82	6563.25	20.71	–2.93	3500.03	0.14	–3.85	0
BP29	11:21:35.3	–43:34:16	0.55	8.65			0.41	4145.97	5.00	0.03	1
BP30	10:54:28.0	–15:59:49	–10.04	9.01			–0.22	4205.23	5.00	0.50	1
			–13.13	8.34			–0.13	4186.30	5.00	0.50	1
BP31	11:49:21.1	–16:07:42	–3.22	9.86			–0.96	3919.75	4.79	–1.12	1
BP32	09:30:18.0	–21:04:54	234.58	10.70	6562.80	0.16	–1.30	4037.45	1.10	–1.69	1
BP33	10:07:07.0	–19:24:04	42.41	8.33			–0.86	3867.57	0.19	–0.98	1
BP34	10:52:49.4	–17:12:15	27.85	9.65			–0.81	3967.24	5.00	–0.01	1
BP35	11:25:38.0	–28:55:53	213.72	22.34	6562.71	–4.06	0.08	4491.12	1.28	–2.18	0
BP36	11:50:27.0	–43:22:29	162.73	86.68			–1.63	3545.06	1.91	–1.51	1
BP37	12:03:52.8	–40:37:26	235.83	23.03			0.23	4481.47	0.85	–1.91	0
BP38	11:37:54.5	–33:58:40	85.07	12.41			–1.01	3982.81	0.55	–1.02	1
BP39	11:45:58.0	–27:13:38	160.08	8.87	6562.46	–15.36	–2.48	3500.02	0.00	–2.68	1
EE06	08:49:19.0	–70:41:50	321.77	7.27			–0.96	3987.77	0.53	–1.00	1
EE07	07:43:44.4	–69:18:05	314.09	10.21			–1.05	3833.99	0.24	–1.64	1
EE08	07:36:51.5	–65:46:52	372.32	7.77			–0.96	4038.42	0.19	–0.96	1
EE09	06:59:30.5	–65:27:18	377.31	7.68			–0.96	3958.61	0.03	–0.94	1
EE10	07:33:06.8	–73:06:27	318.21	9.80			–1.66	3595.92	0.01	–1.07	1
EE11	07:09:52.1	–66:49:31	330.50	21.35			0.03	4496.49	1.28	–0.01	1
EE12	07:13:58.1	–64:19:10	341.07	7.83			–1.11	4020.17	0.59	–1.10	1
EE13	07:22:16.5	–63:42:15	295.71	13.47			0.14	4499.98	0.80	0.00	1
EE14	07:12:18.5	–63:38:09	260.53	80.62			–2.82	3500.01	2.47	–4.78	0
EE15	07:05:00.1	–62:06:39	325.72	13.57	6562.29	–23.48	–1.62	4066.17	1.62	–1.83	1
EE16	06:56:04.7	–63:54:41	279.11	61.28			–2.69	3500.26	0.00	–3.76	0
EE17	08:29:56.1	–70:29:23	182.25	41.15			–1.82	3500.13	1.73	–1.35	1
EE18	08:19:12.4	–66:53:22	162.79	10.26			–0.70	4035.83	0.84	–0.64	1
EE19	06:41:52.5	–62:38:53	312.61	7.92			–1.16	3895.31	0.40	–1.48	1
EE20	08:03:49.1	–63:08:30	357.66	10.26			–0.98	4036.74	0.22	–0.98	1
EE21	07:05:05.6	–61:45:39	381.97	10.93			–1.34	3680.01	0.04	–1.75	1
EE22	09:55:37.2	–71:13:39	150.92	8.40			–0.91	4083.29	1.30	–0.74	1
LA40	09:46:56.8	–82:16:36	248.70	7.78			–1.04	3935.65	0.33	–1.03	1
LA41	08:42:51.7	–83:30:38	220.52	6.90			–1.14	3770.16	0.00	–1.04	1
LA42	08:45:03.8	–81:04:20	269.10	7.26	6562.02	–35.47	–1.15	3831.63	1.10	–1.87	1
LA43	10:14:40.0	–84:36:22	94.74	12.44	6562.79	–0.27	–1.11	3959.30	0.75	–1.42	1
LA44	05:41:39.5	–82:03:02	220.28	10.71	6562.30	–22.95	–1.19	3809.93	1.25	–2.28	1
MS01	05:57:14.3	–53:54:02	317.07	21.15			–0.92	3507.28	0.00	–1.06	1
MS02	07:18:21.2	–55:19:44	254.90	53.34			0.46	4416.97	0.00	–2.96	0
MS03	06:48:06.4	–53:00:33	328.51	24.66	6562.71	–4.20	0.44	4441.20	0.00	–2.52	0
MS04	05:41:38.8	–54:20:09	276.47	13.71	6562.89	3.95	–1.26	3845.89	0.62	–1.92	1
			289.27	13.40	6562.74	–2.72	–1.25	3851.30	0.53	–2.01	1
MS05	06:28:06.1	–53:11:05	302.44	54.11	6562.81	0.56	0.16	4468.77	1.26	–3.22	0

difference. For those objects, we recommend considering the overall metallicity [Fe/H] as only a tentative value.

BP30 and MS04 have been observed twice; in both cases, we derived compatible stellar parameters, T_{eff}, log g, and [Fe/H]. The [Fe/H]$_{\mathrm{CaT}}$ for these two objects is clearly incorrect and could also be explained as a result of their low temperature. In fact, the [Fe/H]$_{\mathrm{CaT}}$ for BP30 is located at the limit of the grid, indicating the code did not find metallicity information within the CaT.

We found a systematically higher difference in the metallicities derived using the Fe lines and the Ca triplet in the presence of H α in emission. In particular, the median difference ([Fe/H] − [Fe/H]$_{\mathrm{CaT}}$) is 0.45 dex for the ten stars in which the H α line is present, while this median difference is only 0.13 dex based on the remaining 27 stars (excluding BP30, as it is at the metallicity limit of the grid). An explanation for this difference could be due to Ca in emission filling in the lines in the triplet, making the metallicities even lower than our code limits. Dependence on the strength of the Ca triplet lines as a function of the strength of the H α line in emission has been reported for a few Mira stars with spectroscopic observations along different phases during the pulsation cycle (Castelaz et al. 2000). Fig. 5 shows

Table 2. Radial velocities from *Gaia* DR3. Radial velocity, its error, and S/N of the spectra are the columns `radial_velocity`, `radial_velocity_error`, and `rv_expected_sig_to_noise`, respectively.

ID	$\mathrm{RV_{Gaia}}$ (km $\mathrm{s^{-1}}$)	RV error (km $\mathrm{s^{-1}}$)	S/N
BP22	306.33	2.15	11.6
BP24	325.88	3.13	7.6
BP25	36.64	3.22	8.1
BP26	100.68	1.81	10.7
BP27	296.57	1.89	11.9
BP28	183.59	1.75	6.1
BP32	230.77	3.14	7.4
BP33	34.17	2.99	7.9
BP35	226.80	1.34	11.4
BP36	206.43	3.65	10.8
BP37	255.94	2.21	10.9
BP38	91.36	2.43	8.4
BP39	156.59	4.12	8.0
EE06	309.69	4.95	6.4
EE10	285.53	3.69	4.5
EE16	346.68	2.15	5.5
EE17	176.06	3.9	8.0
EE18	153.48	3.47	4.5
EE52	125.20	4.87	3.8
LA41	218.32	7.91	3.5
LA42	253.76	4.0	3.1
LA43	95.14	7.84	5.7
LA44	170.08	6.88	3.7
MS02	296.82	1.46	5.5
MS03	349.34	2.41	3.9
MS04	271.02	5.15	4.9

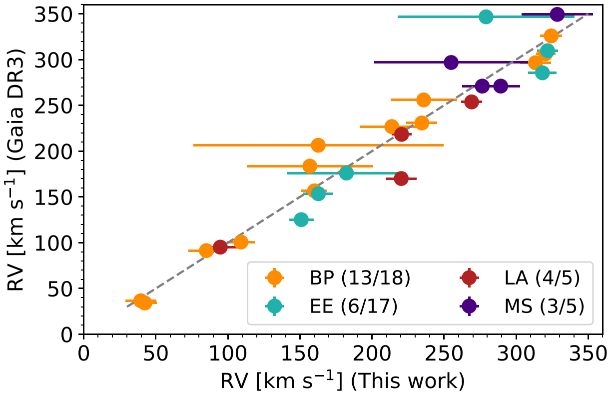

Figure 4. Radial velocity comparison between the values obtained based on COSMOS spectra and *Gaia* DR3 main source catalogue. Stars corresponding to the BP, EE, LA, and MS groups are shown as orange, green, red, and purple circles, respectively. The number in parenthesis in the legend is the number of stars having *Gaia* radial velocities relative to the total number of stars observed in this work.

the [Fe/H] obtained using the Ca triplet and the entire spectrum as a function of the equivalent width of the H α line, when found in emission. The $\mathrm{[Fe/H]_{CaT}}$ metallicities tend to be more lower than the ones based on the entire spectrum, particularly for the stars with equivalent widths of H α greater than 2 Å. Therefore, for those stars in which H α is present, the [Fe/H] estimate based on the Fe lines should be considered as a better estimate of the overall metallicity of the star.

Table 3. Periods for those Mira candidate stars with light curves available in public surveys. *Gaia* periods are derived from the frequency listed in the `gaiadr3.vari_long_period_variable` table for all the stars except for EE10 and EE14, which are only listed in the DR2 corresponding table. Periods in the third column are from either CRTS or ASAS-SN catalogues (see the main text for details).

ID	P_{Gaia} (d)	P_{lit} (d)	Source ID
BP22	366.19	339.90	SSS J101029.1-314452
BP23	122.99		
BP24	103.14	106.53	SSS J111716.7-362011
BP25	121.03	124.26	SSS J102952.7-332925
BP26	407.05	392.42	SSS J103936.2-370853
BP27	116.71	114.01	SSS J102457.2-312547
BP32		103.73	SSS J093018.0-210453
BP33	389.43	413.14	SSS J100707.0-192403
BP35	110.48	111.22	SSS J112538.0-285553
BP36	144.37	145.12	SSS J115027.0-432228
BP37		128.00	ASAS_SN-V J120352.76-403726.3
BP38		64.92	SSS J113754.5-335839
BP39	120.80	119.42	SSS J114558.0-271337
EE06	134.29	132.00	ASAS_SN-V J084919.03-704150.2
EE07	181.09	180.52	SSS J074344.4-691805
EE10	181.55		
EE11	56.62		
EE12	313.12		
EE13		1.13	SSS J072216.5-634214
EE14	286.45	284.90	SSS J071218.6-633809
EE15	112.80		
EE16	225.63	225.00	ASAS_SN-V J065604.73-635441.5
EE17	473.49		
EE19	301.47	324.89	SSS J064152.5-623852
LA40	423.36		
LA41		65.88	ASAS_SN-V J084251.71-833038.3
LA43	132.11		
LA44	156.63		
MS01	398.39		
MS02	36.16	161.06	SSS J071821.2-551943
MS03	158.75	156.39	SSS J064806.4-530033
MS04	139.56	146.65	ASAS_SN-V J054138.80-542008.6
MS05	213.89	219.39	SSS J062806.1-531105

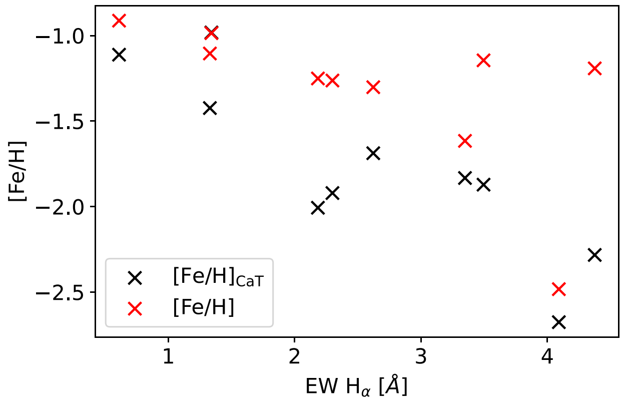

Figure 5. [Fe/H] based on the Ca triplet (black crosses) and Fe lines (red crosses) versus the equivalent width of the H α emission line. The stars tend to be much more metal-poor based on the Ca triplet when the strength of the H α line increases.

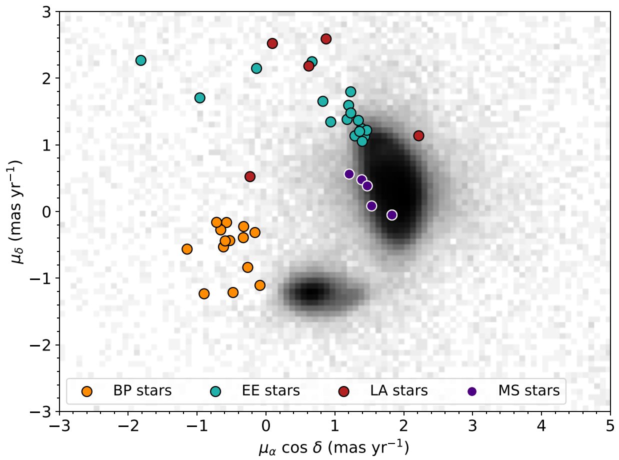

Figure 6. *Gaia* DR3 proper motions for stars up to 10° from the LMC and SMC centres, brighter than G < 17 mag and redder than (BP-RP) > 1.3 mag. Our targets are shown as coloured circles.

Only EE10 has reported astrophysical parameters from the APOGEE-S survey. The spectroscopic metallicity for this star is [Fe/H] = –0.88 ± 0.01, slightly more metal-rich than the metallicity derived based on the Ca triplet. The [Fe/H] value based on Fe lines is much lower, but the effective temperature of this star is low, ∼3500 K, and as mentioned before, the most reliable metallicity estimate in these cases is $[\mathrm{Fe/H}]_{\mathrm{CaT}}$.

The *Gaia* DR3 parallax, effective temperature, surface gravity, metallicity, and spectral types for our targets, when available, are presented in Table A1. The metallicities reported in Gaia DR3 are dominated by large systematic errors, mainly due to a considerable mismatch between models and observed BP/RP spectra (see Andrae et al. 2022). Therefore, the values reported should be taken with due caution. There is a median difference of –0.9 dex between the metallicities reported in this work (based on Fe lines) and the metallicities in Gaia DR3, the latter being systematically more metal-rich.

5 6D PHASE-SPACE INFORMATION

5.1 Parallaxes and proper motions from *Gaia* DR3

Even though most of the observed targets have large radial velocities ($V_{\mathrm{rad}} \geq 200$ km s^{-1}), it is clear that some targets are most likely foreground contaminants ($V_{\mathrm{rad}} \leq 50$ km s^{-1}).

In order to discard those stars and identify potential contaminants with large velocities, parallaxes from *Gaia* DR3 have been analysed. All targets have parallaxes between –0.051 mas to 0.036 mas, with the exception of four stars (BP29, BP30, BP31, and BP34) which have parallaxes > 2 mas (see Table A1). These four stars also have proper motions much larger than the rest of the targets, with absolute values greater than 3 mas yr^{-1} in each component. In addition, these stars have the lowest radial velocities of all the targets – from –11.70 ± 6.12 km s^{-1} (weighted mean of the two measurements for BP30) to 27.85 ± 9.65 km s^{-1} (BP34) – and the highest values of surface gravity ($\log g \approx 5.0$). We therefore exclude these four dwarf foreground stars from the remaining analysis.

Fig. 6 shows the proper motion distribution of our sample, excluding the four contaminants discussed above. The grey scale density corresponds to the comparison sample of stars selected from *Gaia* DR3 and projected within 10° from the LMC's and/or SMC's centres. The comparison stars have G < 17 mag and (G_{BP}–G_{RP}) > 1.3 mag (most likely RGB stars). The main populations of the LMC and the SMC are seen as overdensities at (μ_α, μ_δ) = (1.6, 0.5) mas yr^{-1} and (1.1, –1.15) mas yr^{-1}, respectively. Stars from the MS group have the most similar proper motions to the bulk of the LMC stars, in agreement with previous studies that suggest this northern arc is most likely associated with the LMC disc population (e.g. Cullinane et al. 2022a).

Interestingly, the stars belonging to the BP group have proper motions somewhat different from those of the SMC population. These stars were originally selected as potential debris stars stripped from the SMC, based on their positions in the sky and predictions from simulations of the SMC's disruption under the LMC potential (Deason et al. 2017). It is also possible that a large fraction of the stars in this group are distant Miras in the Milky Way halo, given their brightness and proper motions close to 0 mas yr^{-1}. This group of stars is discussed further in Section 5.4.2.

After removing the likely foreground contaminants based on their parallaxes, proper motions, and radial velocities, our final sample consists of 41 Mira candidates, with measurements of radial velocities and stellar parameters from COSMOS spectra, and parallaxes and proper motions from *Gaia* DR3.

To study the kinematic behaviour of these stars and their possible origin, a distance estimate is needed. However, at the distance of the LMC, *Gaia* parallaxes are not a reliable measurement of distance. In the next section, we discuss different approaches to derive the distance of the stars belonging to the MS, LA, and EE groups (the closest to the LMC in the sky), making use of well-known period–luminosity (PL) relations as well as Magellanic RR Lyrae (RRL) stars as anchors for the distance.

5.2 Light curves and periods

In order to confirm the variable nature of our targets and use their periods, if available, to derive distances, we searched for associated light curves in various datasets. From the *Gaia* time series, 28 of our targets have reported frequencies in either the *Gaia* DR2 or DR3 `vari_long_period_variable` table. The corresponding periods are reported as P_{Gaia} in Table 3. Light curves from the All-Sky Automated Survey for Supernovae (ASAS-SN; Jayasinghe et al. 2018) and from the South Catalina survey (SSS; Drake et al. 2017) were also recovered for 23 variables (5 with light curves and periods not available in *Gaia*). The two most significant periods from the CRTS survey were used to derive phase-folded light curves, adopting the period that allows us to recover one full pulsation cycle. Fig. 7 shows the *Gaia G* or optical *V*-band CRTS or ASAS-SN light curves for MS01, BP37, and MS05. The time series have very different numbers of epochs; nonetheless, the variability is well recovered.

We adopted the periods from CRTS when available, instead of the *Gaia* periods, since the former have a larger number of epochs. When only *Gaia* or ASAS-SN light curves were available, the corresponding period was adopted. The recovered periods range from 35 to 450 d, except for EE13 which has a period of only 1.13 d according to the SSS catalogue. However, the light curve suffers from a considerable scatter and the period reported could be due to a 1-d alias. Therefore, for the remainder of the paper, we consider that a reliable period is not available for this star.

In total, periods were recovered for 32 out of 41 Mira candidates. For the BP, LA and MS groups, a high fraction of the Mira candidates

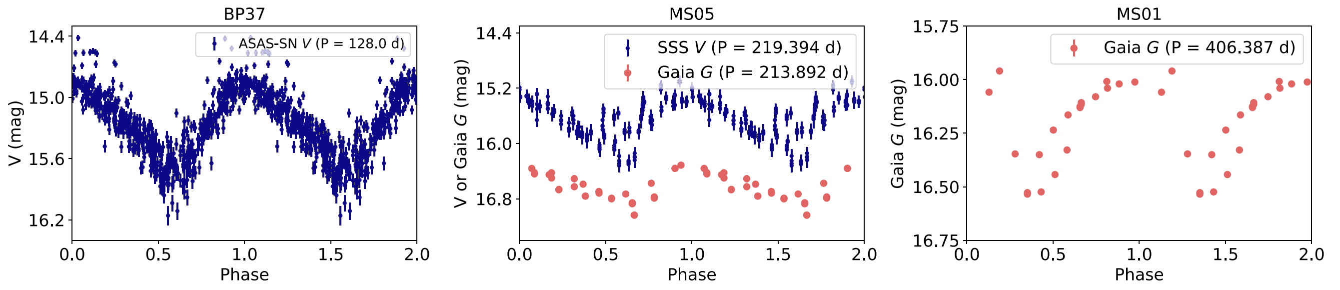

Figure 7. *Gaia G* and optical *V*-band light curves for three Mira candidate stars in our sample. From left to right: ASAS-SN optical *V*-band light curve and period for BP37; periods and light curves from the *Gaia* and CRTS surveys for MS05; and *Gaia G*-band light curve and period for MS01.

has reported periods. In the case of the EE stars, light curves were found for 10 (out of 17) stars. As a result, only for a subsample of them, distances can be derived using any of the PL relations for LMC stars (see e.g. Soszynski et al. 2007). We proceed to separate this subsample into C-rich and O-rich Miras, and fundamental, first-overtone, and long-secondary period pulsators, to apply the corresponding PL relation and derive their distances.

5.3 Photometric chemical types

Among long-period variables (LPVs), different masses and types of stars can be found. Depending on the evolutionary stage (RGB or AGB star), mass regime, and surface chemistry (C/O-rich), these stars follow different $K_{\rm S}$–PL and *Gaia G*–PL relations (Lebzelter et al. 2019). The $K_{\rm S}$–PL diagram for LPVs in the LMC shows different relations for C-rich and O-rich red giants, as well as for fundamental and first-overtone pulsating Miras, semiregular variables and long-secondary period variables (see e.g. Soszynski et al. 2007). Therefore, identifying the subtype of each of the targets in our sample is necessary in order to derive distances for those stars with measured periods (see Section 5.2).

A powerful diagram to separate the different subtypes of pulsating giant stars is the ($W_{\rm RP} - W_{\rm J,\,Ks}$) versus $K_{\rm S}$ diagram presented by Lebzelter et al. (2018). Combining optical *Gaia G*, $G_{\rm BP}$, $G_{\rm RP}$ magnitudes and near-IR 2MASS J and $K_{\rm S}$ magnitudes, the Wesenheit functions $W_{\rm RP}$ and $W_{\rm J,\,Ks}$ allow us to use reddening-free magnitudes. Lebzelter et al. (2018) defined a boundary to separate C-rich from O-rich LPVs in the LMC based on the ($J - K_{\rm S}$) colours, with C-rich stars being those with redder near-IR colours (i.e. having $W_{\rm RP} - W_{\rm J,\,Ks} \gtrsim 0.8$ mag). Among the O-rich stars, using population synthesis models, Lebzelter et al. (2018, 2019) defined different boundaries to separate low, intermediate and high-mass pulsating AGB stars, while the faintest O-rich stars ($K_{\rm S} \geq 12$ mag) are mostly early AGB and RGB stars from the tip of the RGB in the LMC.

We cross-match our targets with the *Gaia* DR3 and 2MASS catalogues, using a search radius of 1.0 arcsec. The Wesenheit functions were calculated following the original definition in Lebzelter et al. (2018), as follows:

$$W_{\rm BP,RP} = G_{\rm RP} - 1.3\,(G_{\rm BP} - G_{\rm RP})\,, \tag{1}$$

$$W_{\rm J,Ks} = K_{\rm S} - 0.686\,(J - K_{\rm S})\,. \tag{2}$$

Fig. 8 shows the location of our target stars (from the three groups close to the LMC: MS, EE, and LA) in the ($W_{\rm RP} - W_{\rm J,\,Ks}$), $K_{\rm S}$ diagram. The boundaries from Lebzelter et al. (2019) are shown as dashed lines, while the corresponding subtypes are shown as green (O-rich RGB and faint, early AGB stars), blue (O-rich low-mass AGB stars), cyan (O-rich intermediate-mass AGB stars), red (C-rich), and yellow (extreme C-rich) circles. None of our targets has colours and magnitudes in the location of red supergiants (RSGs) or O-rich massive AGB stars. We find that most (22 out of 27) of our targets are O-rich stars, while five are C-rich including one extreme C-rich star (though note that two stars have colours on the boundary between C- and O-rich groups). Among the O-rich stars, nine have colours and magnitudes consistent with RGB stars or faint, early AGB (green circles); one star (cyan circle) has properties consistent with being an intermediate-mass (initial stellar masses, $M_{\rm i} \gtrsim {\sim}2.0$ to ${\sim}3.2$ M$_\odot$) AGB star; and the remainder (12 out of 27) are consistent with being O-rich low-mass ($M_{\rm i} \sim 0.9$ to ${\sim}1.4$ M$_\odot$) early AGB or thermal-pulsating AGB stars.

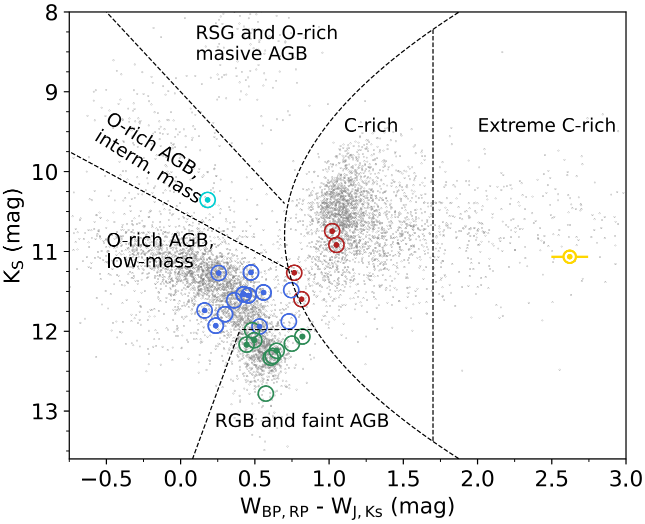

Figure 8. $W_{\rm BP,\,RP} - W_{\rm J,Ks}$ versus $K_{\rm S}$ diagram for LPV stars around the LMC (grey dots) as well as the Miras-like stars belonging to the EE, MS, and LA groups. The boundary lines that separate C-rich from O-rich stars, as well as the different mass regimes, are marked as dashed lines (taken from Lebzelter et al. 2019). Our sample is mainly comprised of O-rich low-mass AGB stars. Those stars with periods available in the literature are denoted with a coloured dot inside the marker.

Eighteen out of the 27 stars in Fig. 8 have periods available, and distances can thus be estimated using PL relations.

The targets from the BP group were not included in this diagram since the boundaries from Lebzelter et al. (2018) are defined for the LMC distance modulus. The Mira stars in the BP group are far from the Clouds and their distances could be quite different from the LMC. We discuss this particular group in the next section.

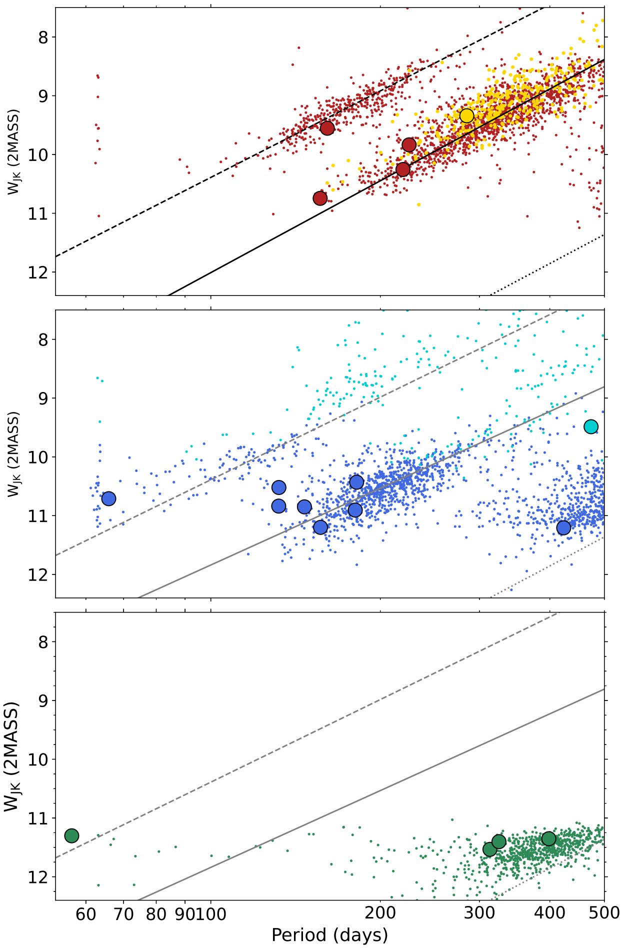

Figure 9. Wesenheit index $W_{\mathrm{J,\,Ks}}$–PL diagrams for LPVs in the LMC, colour-coded according to their classification in the *Gaia*-2MASS diagram (see Fig. 8). In the top panel, C-rich (red) and extreme C-rich (yellow) stars are shown, along with the five of our targets found to be consistent with this classification. The middle panel shows those stars classified as O-rich AGB stars of low (blue) and intermediate (cyan) mass, while the bottom panel presents the RGB and faint AGB stars (green). The best-fitting PL relations for the first-overtone, fundamental-mode, and long-secondary period sequences are shown as dashed, solid, and dotted grey/black lines for O/C-rich stars, according to Soszynski et al. (2007).

5.4 Distance determination

5.4.1 Stars around the LMC

Following the classification into subtypes from Lebzelter et al. (2019), we divided the Mira candidate stars around the LMC into C-rich stars, O-rich stars, and RGB or faint AGB stars (with magnitudes consistent with the tip of the LMC's AGB). The top panel of Fig. 9 shows the Wesenheit $W_{\mathrm{J,\,Ks}}$–period diagram for those stars classified as extreme C-rich (yellow points) and C-rich (red points); the middle panel shows the O-rich low (blue) and intermediate-mass (cyan) AGB stars, and the bottom panel includes only the stars consistent with being RGB or faint AGB stars (green points). The larger coloured points correspond to our targets (one extreme C-rich, four C-rich, eight O-rich low-mass, one O-rich intermediate-mass and four RGB/faint AGB stars), while the smaller coloured dots correspond to LPVs variables in the LMC, selected following the same selection criteria as in Lebzelter et al. (2018), and cross-matched with the 2MASS photometry. In each panel, the best-fit PL relations from Soszynski et al. (2007), based on the Optical Gravitational Lensing Experiment (OGLE) observations, are shown for first-overtone pulsators (dashed lines), fundamental mode pulsators (solid lines) and long-secondary period variables (dotted lines), for both O-rich (grey) and C-rich (black) red giant variables.

As already noted by Lebzelter et al. (2019), there is significant scatter and deviations from the best PL relations in all pulsation modes, reflecting inaccurate 2MASS mean magnitudes (one single measurement over the pulsation period) as well as underestimated periods, shifting the distribution of LMC LPVs towards shorter periods. This effect is clearly seen in the case of the RGB and faint AGB stars (bottom panel in Fig. 9), which are found mostly pulsating in the long-secondary period (the stars with the longest periods in the sample), and which are systematically offset from the PL relation. In fact, all the stars with the longest (>300 d) periods in our sample – i.e. EE12, EE19, MS01, LA40, and EE17– are systematically offset from the PL relation of the most likely pulsation mode. Therefore, these LPVs cannot be used as precise distance estimators unless the time-series photometry is sufficient to recover reliable period estimates.

In the case of the extreme C-rich stars (yellow points, top panel of Fig. 9), these are expected to be pulsating in the fundamental mode. Nonetheless, there is considerable scatter in their magnitudes with respect to the corresponding PL sequence derived by Soszynski et al. (2007). This scatter can be due to stars that are highly reddened and/or stars producing high-opacity dust grains.

If all our targets were of the Mira variability class, they should be pulsating in the fundamental mode. Nonetheless, given the selection made to identify these, we cannot rule out that some of our targets are instead semi-regular variables which could be pulsating in the fundamental or first-overtone pulsation modes. In fact, as Fig. 9 shows, stars with large periods ($P > 300$ d) tend to be in the locus for those stars in the long-secondary period group (green dots), while stars with short periods ($P < 100$ d) preferentially pulsate in the first-overtone mode. Assuming that each of our targets is pulsating in the pulsation mode corresponding to the closest relation in Fig. 9, we derived their distance moduli using the Wesenheit $W_{\mathrm{J,\,Ks}}$–PL relations from Soszynski et al. (2007). To obtain the individual distances, a distance modulus of 18.477 ± 0.004 (statistical) $\pm$ 0.026 (systematic) mag (Pietrzyński et al. 2019) for the LMC was adopted.

In the case that all our targets are Miras, pulsating in the fundamental mode, the distances would be ~2 times shorter (~ 4 times larger) for those stars considered to be pulsating in the first-overtone (long-secondary period). This scenario is unlikely, however, as our targets are close to the LMC in the sky and it is more plausible to find distant (~50 kpc) long-period (Mira-like) variables around the LMC periphery than finding Milky Way halo Miras at less than 30 kpc close to the LMC, or Mira candidates at distances more than 200 kpc.

In order to confirm the order of magnitude of the distances obtained with the limited information we have about our targets' pulsation mode, Fig. 10 shows the distances obtained for our targets on top of the distribution of the Magellanic RRL stars. The top and middle panels show the distance of our targets based on the PL relations and the median distance of the 5 RRL closest on the sky to each of our targets. The bottom panel shows the standard deviation in the RRL distance. The figure shows that RRLs trace substructures around our targets from 42 to 52 kpc, with a mean distance of 45 kpc (with median error bars of less than 5 kpc). While our targets are at distances from 36 kpc to 65 kpc, their mean distance is ~ 46 kpc, as in the case of RRLs.

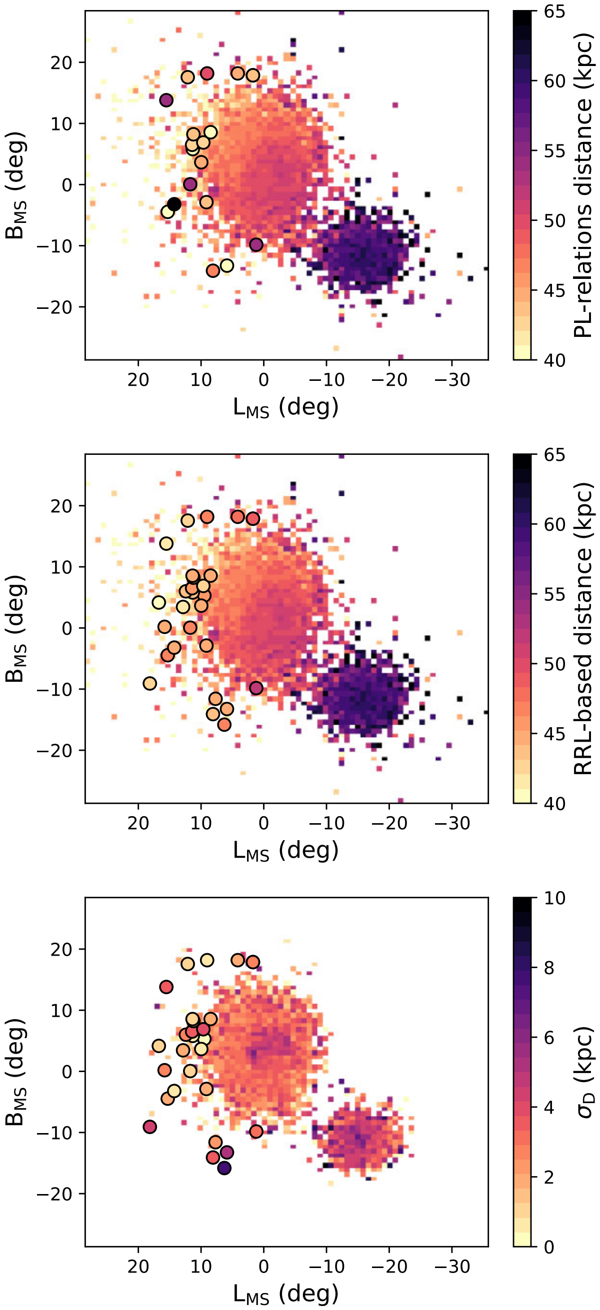

Figure 10. Heliocentric distances for different stellar tracers around the Clouds. The 2D histogram shows the mean distance (top and middle panels) of RRL stars around the Clouds and its standard deviation (bottom panel). The top panel shows as coloured circles those targets with available distances, based on PL relations. The middle and bottom panels show the mean heliocentric distances and standard deviation for RRL stars, respectively, around the on-sky position of our targets.

Table 4 gives the different subtypes for our targets based on Fig. 8 (i.e. C-rich or low-mass, intermediate-mass, and RGB O-rich stars), their pulsation mode based on Fig. 9, and their associated distance. For those stars at the boundary of being O-rich/C-rich (MS03 and MS05), both possible distances are reported. In the case of LA43, its position in $W_{J,\,K_s}$ – PL diagram is between the fundamental mode and first overtone relations, and therefore both possible distances are reported.

Table 4. Heliocentric distances from PL relations. The subtypes (C- or O-rich, low-mass, intermediate-mass, or RGB) for those stars with available periods are presented. The pulsation mode (FM: fundamental mode, FO: first-overtone, LSP: long-secondary period) adopted to derive distances is also included. Distance errors are obtained from the propagation of uncertainties on the PL relation coefficients, LMC distance modulus, and 2MASS magnitudes.

ID	Subtype	Pulsation mode	Distance (kpc)
EE06	O-rich (low)	FM	39.8 ± 1.2
EE07	O-rich (low)	FM	53.9 ± 1.7
EE10	O-rich (low)	FM	43.5 ± 1.3
EE11	O-rich (RGB)	FO	44.4 ± 1.1
EE12	O-rich (RGB)	LSP	37.7 ± 1.4
EE14	Extreme C-rich	FM	43.0 ± 1.9
EE15	O-rich (RGB)	FM	43.5 ± 1.3
EE16	C-rich	FM	42.3 ± 1.7
EE17	O-rich (mid)	FM	64.7 ± 2.6
EE19	O-rich (RGB)	LSP	36.7 ± 1.5
LA40	O-rich (low)	LSP	42.9 ± 1.8
LA41	O-rich (low)	FO	38.9 ± 1.0
LA43	O-rich (low)	FO/FM	34.4 ± 1.0/ 68.3 ± 1.7
LA44	O-rich (low)	FM	54.5 ± 1.8
MS01	O-rich (RGB)	LSP	43.4 ± 1.8
MS02	C-rich	FO	53.8 ± 1.6
MS03	C-rich/O-rich (low)	FM	44.1 ± 1.6/44.2 ± 1.3
MS04	O-rich (low)	FM	43.8 ± 1.3
MS05	C-rich/O-rich (low)	FM	50.0 ± 2.1/47.3 ± 1.6

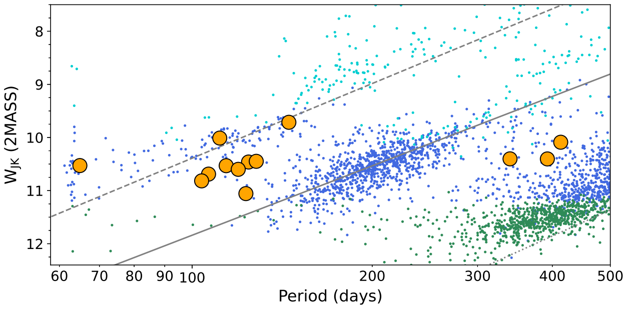

Figure 11. Period–magnitude diagram for the stars located above the Galactic plane. The PL sequences for first-overtone (dashed line), fundamental-mode (solid line), and LSP (dotted line) LPV stars in the LMC are included. The distribution of LPV stars in the LMC are shown as blue, cyan, and green symbols as in Fig. 9.

5.4.2 *Stars above the Galactic plane (BP group)*

Among our targets, after discarding the four foreground stars with large parallaxes, there are 14 Mira candidates located above the Galactic plane. Given their position on the sky, these stars could be unrelated to the Clouds, and distance determination is thus more uncertain.

Most of these stars do, however, have periods available (see Table 3) which can in principle be used to derive distances. Fig. 11 shows the position of these stars in the period–$W_{J,\,K_s}$ diagram, as well as the best PL sequences for O-rich LPVs around the LMC. In contrast with the stars discussed in Section 5.4.1, these stars can be easily at less than 30 kpc (i.e. be bright stars pulsating in the fundamental mode) and no assumptions can be made regarding their pulsation modes. We therefore report the two most likely distances

Table 5. Heliocentric distance estimates for the BP stars. The distances for two possible pulsation modes are reported. Errors on the distances are obtained by propagating the uncertainties as in Table 4.

ID	Pulsation mode	Distance (kpc)	Pulsation mode	Distance (kpc)
BP22	FM	74.0 ± 2.7	LSP	24.2 ± 0.9
BP23	FM	41.4 ± 1.1	FO	81.8 ± 1.8
BP24	FO	60.4 ± 1.5	FM	30.8 ± 0.9
BP25	FO	62.8 ± 1.6	FM	31.7 ± 0.9
BP26	FM	83.8 ± 3.2	LSP	27.6 ± 1.1
BP27	FO	59.8 ± 1.4	FM	30.4 ± 0.8
BP32	FO	62.5 ± 1.5	FM	32.0 ± 0.9
BP33	FM	75.9 ± 2.9	LSP	25.1 ± 1.0
BP35	FO	46.0 ± 1.1	FM	23.4 ± 0.7
BP36	FO	51.4 ± 1.3	FM	25.7 ± 0.8
BP37	FO	64.2 ± 1.5	FM	32.4 ± 0.9
BP38	FO	35.3 ± 0.9	FM	18.6 ± 0.6
BP39	FO	64.5 ± 1.6	FM	32.7 ± 1.0

(based on how close each star is to the different PL sequences) in Table 5.

Given the uncertain distances for these stars, and their proper motions centred on $(\mu_\alpha, \mu_\delta) = (0, 0)$ mas yr^{-1}, we cannot rule out the possibility of them being foreground (∼ 30 kpc) Galactic Mira-like stars, rather than being associated with the LMC or SMC. This group of stars *is* located close to the predicted area of the sky where tidally stripped LMC RRL stars have been reported by Petersen, Peñarrubia & Jones (2022). However, based on the mock observations presented in Petersen et al. (2022), LMC debris is expected to have much larger line-of-sight velocities than that measured for the BP stars ($V_{\mathrm{los}} > 300$ km s^{-1}). Further investigation to understand the origin of the BP stars (as likely distant Galactic Mira-like stars) is needed, however, it is beyond the scope of this work. Accordingly, for the remainder of this paper, we will focus on the Mira candidates in the vicinity of the Clouds.

6 OUTER PERIPHERY OF THE LMC

In the following sections, the phase-space measurements for the three groups (towards the north, east, and south of the LMC) of Mira-like stars in the vicinity of the Clouds are analysed and compared to previous measurements.

6.1 Spectroscopic metallicities

Based on the COSMOS data, there are 21 stars with reliable spectroscopic [Fe/H] (`flag` = 1) in the vicinity of the Clouds. We adopt the [Fe/H] based on the Ca triplet for all the stars that do not show H α in emission, while for the rest, the overall [Fe/H] was preferred (see Section 4.2).

For the stars in the MS group, only two metallicity measurements are available (MS01 and MS04), being in good agreement with the reported metallicities for the northern arm in Cullinane et al. (2022a). Fig. 12 shows the metallicity distribution of the stars in the EE group and the mean metallicities and standard deviation for the stars in the MS ([Fe/H]=–1.16, σ = 0.10 dex) and LA groups ([Fe/H]=–1.10, σ = 0.06 dex) as horizontal lines. For reference, the metallicity distribution of stars in the LMC inner disc (within 8° from the LMC centre, dashed line), in the outer disc (more than 8° from the LMC centre, dotted line), and in the SMC disc (up to 7° from its centre) based on APOGEE observations (see e.g. Cheng et al. 2022) is also shown. The mean metallicity of MS and LA stars is ∼0.5 dex more metal-poor than the peak of the metallicity distribution of the LMC stars, but consistent with the metal-poor tail of the outer disc.

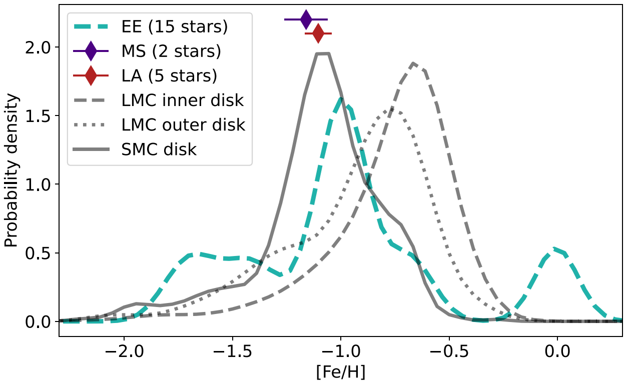

Figure 12. Metallicity distribution function for the stars in the EE group (green dashed line), LMC inner (dotted grey) and outer (dashed grey) disc stars, and SMC disc stars (solid grey line). The mean metallicity of the MS and LA stars are shown as purple and red diamonds, respectively, with error bars corresponding to the standard deviation of the mean.

The metallicity distribution function of the EE stars shows three different peaks, the most prominent of them located at [Fe/H] = –1.0, consistent with MS and LA stars. There are two metal-rich stars and a more extended metal-poor tail, with a peak at [Fe/H]=–1.6. Similar results have been reported in Cheng et al. (2022) and Cullinane et al. (2022a, b), consistent with a more metal-poor population in the periphery of the Clouds, which is both compatible with the metal-poor end of the LMC disc metallicity distribution or SMC population, which cannot be fully ruled out. However, given the kinematics of the stars in our sample, they are most likely metal-poor LMC disc stars.

6.2 Radial velocities, proper motions, and distances

Fig. 13 shows the phase-space information available for the targets in the three different groups of stars in the Magellanic periphery. The on-sky position as well as radial velocities, proper motions and distances, are shown. The angle ϕ is used as a position angle, going from 0 to 180° anticlockwise from North towards South. In the bottom row, the mean distance of the closest RRL is presented as a grey symbol. In this figure, it is possible to recognize trends and isolate potential outliers for each group.

In the case of the MS stars (left-hand panels), the target at the largest on-sky distance with respect to the LMC centre (MS02, ϕ = 60°) has a rather smaller radial velocity and potentially deviating distance compared to the rest of the stars in the group. As a comparison, the left-hand panels include the measurements presented by Cullinane et al. (2022a) for different fields along the northern arm (violet triangles). It is clear that our targets trace the same trends in radial velocity and proper motions as in Cullinane et al. (2022a), with MS02 most likely being an outlier. The trend in distances, being those stars at large ϕ slightly more distant than those close to the LMC centre, can be explained considering the inclination and orientation of the line of nodes of the LMC plane, as already discussed in Cullinane et al. (2022a).

For the LA stars (right-hand panels), there seems to be one outlier based on its rather small radial velocity and proper motions (LA43, ϕ = 165°). LA 44, at ϕ = 176°, also has a deviating proper motion

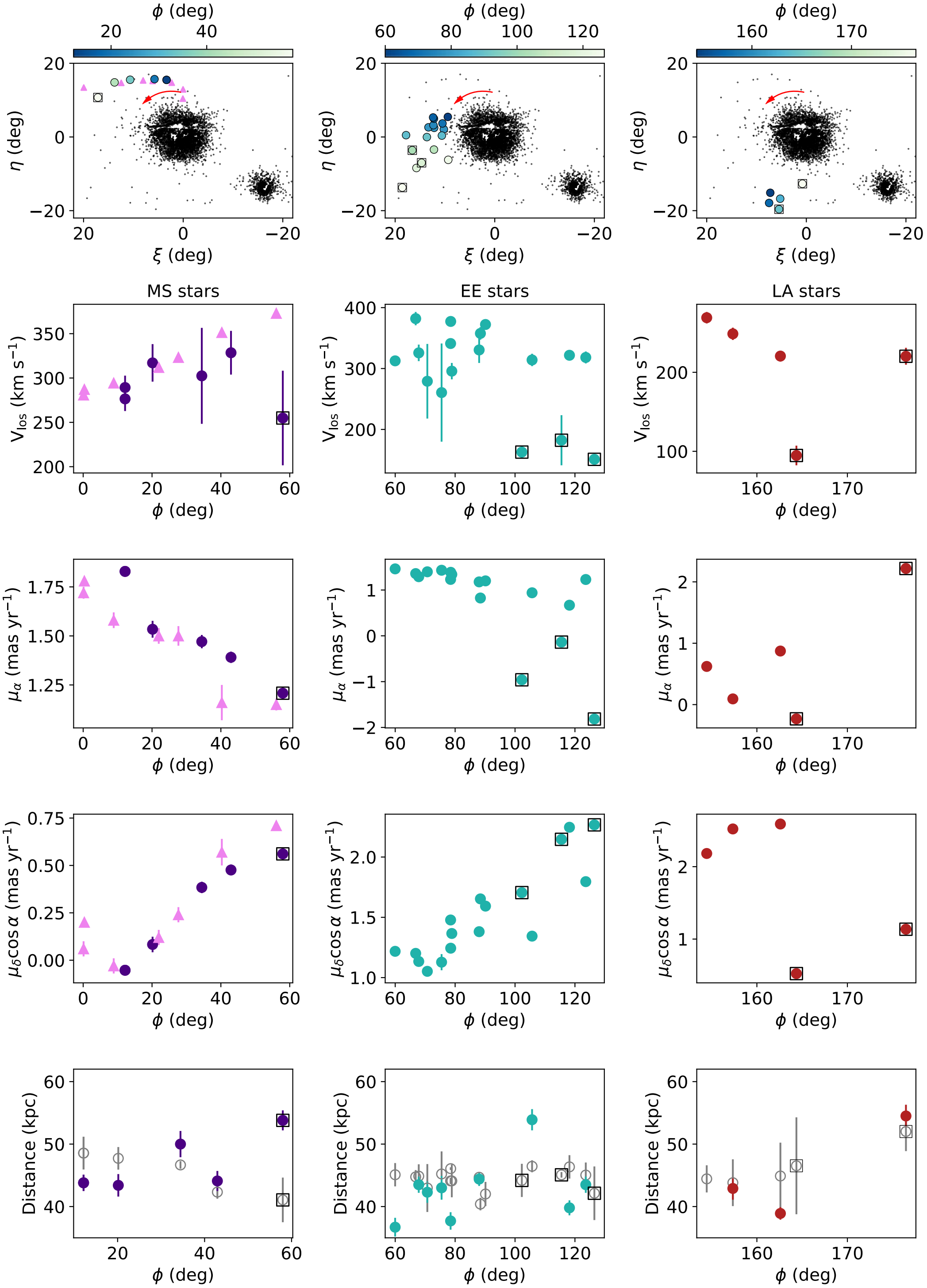

Figure 13. Phase-space properties for our targets. The left, middle, and right panels correspond to stars in the MS, EE, and LA groups. The top panels show the on-sky distribution of the Mira candidates selected by Deason et al. (2017). The rec arrow shows the direction of the ϕ position angle. In the left panels, the violet triangles are measurements from Cullinane et al. (2022a) for different fields along the LMC northern arm. Distances derived based on PL relations are shown as coloured circles, while those corresponding to the mean distance of the closest RRL stars are shown as grey open circles. Possible kinematic outliers for each group are denoted with open square outlines in each panel.

compared to the rest of the stars in the group. We therefore consider both as potential contaminants.

In the case of EE stars (middle panels), most of the stars have large (> 300 km s^{-1}) velocities, except for three stars: EE17, EE18, and EE22. These stars are located at the largest on-sky distances from the LMC centre. Their proper motions, particularly $\mu_{\alpha *}$, also deviate from the other stars in the group. We decided to flag them as potential outliers, although it could be that these stars are instead tracing a different structure, as they all have very similar, relatively large velocities (> 150 km s^{-1}).

6.3 3D motions

With 6D phase-space information in hand, the 3D motion for each star in the LMC reference frame can be calculated. In particular, the cylindrical velocities ($V_{\rm R}$, V_ϕ, and V_Z) can be used to assess the origin (e.g. disturbed LMC disc stars) of our targets. Based on the van der Marel & Cioni (2001) and van der Marel et al. (2002) formalism, the radial motion $V_{\rm R}$, azimuthal motion V_ϕ, and the velocity perpendicular to the disc plane $V_{\rm Z}$, can be estimated as

$$\begin{aligned} V_{\rm R} &= \left(x' v_x' + y' v_y'\right)/R, \\ V_\phi &= \left(y' v_x' - x' v_y'\right)/R, \\ V_{\rm Z} &= v_z'. \end{aligned} \tag{3}$$

R is the in-plane radial distance of a tracer to the LMC centre, while (v_x', v_y', v_z') are the Cartesian velocities in the plane of the LMC disc, after subtracting the LMC systemic motion. To derive these Cartesian velocities, the formalism introduced by van der Marel & Cioni (2001) and van der Marel et al. (2002) was followed. The LMC centre-of-motion (COM) was fixed at (α_0, δ_0) = (79$.\!\!^\circ$88, −69$.\!\!^\circ$59) (van der Marel & Kallivayalil 2014), while the line-of-sight velocity and the proper motions of the COM used were $V_{\rm los} = 261.1$ km s^{-1}, and ($\mu_\alpha \cos\delta$, μ_δ) = (1.895, 0.287) mas yr^{-1}, from van der Marel & Kallivayalil (2014). The adopted LMC heliocentric distance was $D_{\rm H}$ = 49.5 kpc (Pietrzyński et al. 2019). For the LMC disc geometry, the values reported by Choi et al. (2018) were used, following the discussion in Cullinane et al. (2022a): i.e. $i = 25.\!\!^\circ86$ and $\theta = 239.\!\!^\circ23$, respectively.

We adopted the distances of the closest RRL stars in the sky as a rough estimate of the distance of each Mira candidate, even for those without periods available in the literature. As shown in Fig. 10, for those stars with available periods, the distance derived using PL-relations for long-period variables in the LMC and those obtained based on the closest RRL stars are compatible. To test the influence of the distance determination used, we also computed the cylindrical velocities assuming that all our targets are on the LMC disc plane (z' = 0 kpc), and therefore their on-plane distance is derived as

$$D_{\rm disk} = \frac{D_0 \cos i}{\cos i \cos\rho - \sin i \sin\rho \sin(\phi - \theta)}, \tag{4}$$

where (ρ, ϕ) are the on-sky distance and position angle of our targets, respectively. The cylindrical velocities obtained this way are, for most of the stars, compatible within the errors with those values derived adopting the RRL-based distance. However, for the stars at a large projected radius R, the vertical position z' could significantly deviate from the disc plane. Fig. 14 shows the in-plane projected radius R of each star and the corresponding vertical position z$'$, estimated based on the RRL-based distance, which is positive for stars above the LMC disc (in the direction towards the observer). Stars located at $R > 14°$ are located more than 5 kpc away from the LMC disc, in agreement with the results for red-clump stars presented in Cullinane et al. (2022b). Therefore, we adopted the individual distances for each star instead of assuming that all of them are located in the LMC disc plane. The gnomonic-projected coordinates (η, ξ) and 3D velocities are presented in Table 6, including the corresponding errors derived from the propagation of the uncertainties in the measured proper motions, radial velocities and distances.

Fig. 15 shows the V_ϕ (left-hand panel), $V_{\rm R}$ (middle panel), and $V_{\rm Z}$ (right-hand panel) for all our targets. It is evident that the largest variations in velocity are found at the largest angular distances from the LMC (i.e. outer EE and LA stars). The azimuthal velocity is consistent with $V_\phi \sim 70$ km s^{-1}, which is the constant value reached by the LMC rotation curve (see e.g. Wan et al. 2020; Gaia Collaboration 2021; Cullinane et al. 2022b; Jiménez-Arranz et al. 2023) for most of the stars, particularly those in the northern arm. A few stars have excessively large azimuthal velocities, of the order of 300 km s^{-1}, corresponding to those with line-of-sight velocities < 200 km s^{-1}, while one of the LA stars has a counter-rotating motion. These deviating azimuthal velocities could be due to perturbations in the outer LMC.

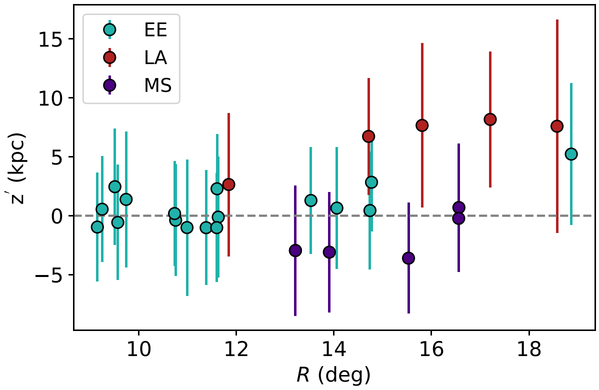

Figure 14. In-plane radial distance R versus vertical distance z' for the stars in the vicinity of the LMC. Beyond ∼15°, the stars are far from the LMC disc plane.

Table 6. 3D cylindrical velocities in the LMC coordinate system.

ID	ξ (deg)	η (deg)	V_ϕ (km s^{-1})	$V_{\rm R}$ (km s^{-1})	$V_{\rm Z}$ (km s^{-1})
EE06	15.2	–7.9	135.9 ± 5.5	43.9 ± 6.0	33.8 ± 6.6
EE07	11.5	–3.0	33.3 ± 7.8	–48.5 ± 7.9	–13.1 ± 9.4
EE08	12.7	0.4	48.1 ± 8.2	37.1 ± 8.2	–39.9 ± 7.9
EE09	9.3	2.4	38.4 ± 8.2	39.6 ± 8.7	–60.8 ± 7.9
EE10	8.7	–5.9	85.2 ± 6.8	–5.3 ± 7.8	–26.8 ± 9.0
EE11	9.7	0.7	81.5 ± 11.9	0.4 ± 8.7	–38.6 ± 18.9
EE12	11.2	2.8	86.5 ± 8.2	44.1 ± 8.1	–29.2 ± 7.9
EE13	12.3	3.0	68.2 ± 8.8	23.6 ± 7.5	36.5 ± 12.1
EE14	11.3	3.5	55.0 ± 39.3	–3.8 ± 21.7	69.0 ± 70.2
EE15	11.2	5.3	66.9 ± 8.1	11.5 ± 6.5	–7.9 ± 12.2
EE16	9.5	4.0	72.7 ± 27.6	–12.4 ± 12.2	22.6 ± 54.1
EE17	14.1	–6.5	222.5 ± 14.7	–189.2 ± 21.5	4.2 ± 32.7
EE18	15.8	–3.1	321.5 ± 6.8	–305.5 ± 6.4	–78.6 ± 8.9
EE19	8.4	5.7	78.6 ± 7.8	61.6 ± 7.5	–12.9 ± 7.9
EE20	16.9	1.1	82.6 ± 7.9	10.2 ± 7.0	–23.4 ± 9.2
EE21	11.3	5.6	39.4 ± 7.7	43.5 ± 6.8	–49.6 ± 10.1
EE22	18.2	–13.0	283.1 ± 5.4	–314.1 ± 6.8	–81.4 ± 7.1
LA40	7.3	–17.7	81.9 ± 5.7	–41.2 ± 6.4	20.5 ± 6.9
LA41	5.1	–16.6	122.1 ± 6.5	–73.0 ± 6.6	34.7 ± 6.8
LA42	7.0	–14.9	43.8 ± 6.7	–40.2 ± 6.7	–9.1 ± 6.9
LA43	5.4	–19.5	–357.4 ± 6.5	–52.0 ± 8.0	64.1 ± 9.9
LA44	0.4	–12.8	133.4 ± 7.8	–102.6 ± 8.0	–1.5 ± 9.9
MS01	4.3	15.8	51.9 ± 15.8	–48.5 ± 15.6	–16.1 ± 51.1
MS02	15.8	11.2	96.5 ± 22.1	–99.8 ± 18.1	64.5 ± 45.8
MS03	12.3	15.2	67.1 ± 9.7	–40.8 ± 9.6	–6.6 ± 22.1
MS04	1.9	15.5	–2.9 ± 6.0	–50.1 ± 6.0	2.3 ± 11.1
MS05	9.2	15.8	47.7 ± 9.2	–25.4 ± 9.0	–0.4 ± 19.5

The in-plane radial velocity, V$_R$, mildly deviates from a disc in equilibrium for several stars. In the case of those stars in the northern

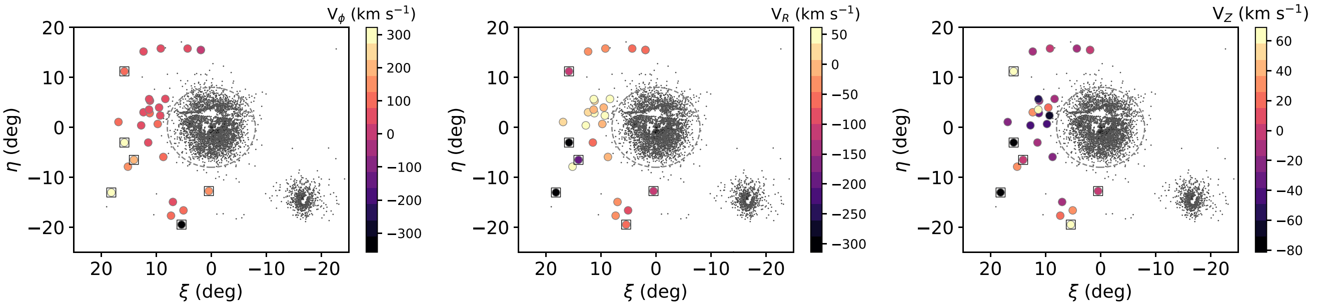

Figure 15. The azimuthal velocity (V_ϕ), radial velocity (V_R), and vertical velocity (V_Z) for our targets. The dashed circle marks 9° from the LMC centre. The black points are the Mira candidates from Deason et al. (2017). The potential kinematic outliers, based on their radial velocities and proper motions, are marked with open squares.

arm (MS), an inward motion of ~ -46 km s^{-1} is found, consistent with the measurements of Cheng et al. (2022) and Cullinane et al. (2022a). For the outer EE stars and LA stars, however, V_R reaches much larger values, up to -250 km s^{-1}, reinforcing the idea of these being perturbed LMC disc material. Large inward velocities were also reported by Cheng et al. (2022) towards the south of the LMC.

The possible outlier in the MS group, MS02 (see Fig. 13), is located slightly off from the track of the northern arc, inside the so-called 'North-East Structure' (NES; Gatto et al. 2022). Based on proper motions from *Gaia*, the NES was found to have in-plane velocities V_R, V_ϕ similar to the stars in the northern arm, suggesting a possible common origin. We found, however, that the out-of-plane velocity V_Z strongly deviates from the values for the rest of MS stars, which are consistent with a disc in equilibrium. The out-of-plane velocities, $\mathrm{V_Z}$, of other stars, largely deviate from a disc in equilibrium, reaching up to -80 km s^{-1} (EE22).

Similar to the results in Cullinane et al. (2022a), the out-of-plane velocities for the MS stars appear to be out of equilibrium. However, owing to the large errors in radial velocities for the MS stars, the error on V_Z does not allow us to confirm this behaviour. As those stars in the N1 and N2 fields of Cheng et al. (2022), the radial and rotational motion of these stars is compatible with a disc origin. Cullinane et al. (2022a) found consistent velocities in the seven fields tracing the northern arm (see dashed blue circles in Fig. 1), finding that the stars in them have a mean V_ϕ of the order of $\sim$70 km s^{-1}, consistent with the rotation curve of the LMC. On contrast, V_R and $\mathrm{V_Z}$ are deviated from zero, expected for a disc in equilibrium. The five MS stars have an inward radial motion of $\sim$40 km s^{-1}, similar to the value derived in Cullinane et al. (2022a). Therefore, the MS stars are consistent with LMC disc stars, most likely out of equilibrium.

The 3D velocities of the EE stars in the northern-east area (η, $\xi > 0°$) are consistent with a perturbed disc, having a median azimuthal velocity of $V_\phi \sim 65$ km s^{-1}, in-plane radial velocities V_R going from almost zero up to $\sim$60 km s^{-1}, and mostly negative out-of-plane velocities. These relatively large in-plane radial and out-of-plane velocities are contrary to the findings of Cullinane et al. (2022b), based on the aggregate motion of red clump stars in three fields at the north-east of the LMC, which were found to be consistent with a disc in equilibrium. This apparent disagreement can potentially be due to the larger angular separations from the LMC centre traced by the EE stars (from to 16° up to $\sim$21°) compared to the fields in Cullinane et al. (2022a) (see Fig. 1).

For the EE stars in the southern-east region, the azimuthal and in-plane radial velocities are exceedingly large, reaching out to $V_\phi \gtrsim 300$ km s^{-1} and $V_\mathrm{R} \sim -300$ km s^{-1}. These large 3D velocities can be explained based on the different line-of-sight velocities and proper motions of these stars, see the middle panels in Fig. 13. The three potential outliers have relatively large line-of-sight velocities (> 150 km s^{-1}) but are considerably lower than the rest of the stars in the EE group. The proper motions in the R.A. direction also strongly deviate from the values for stars in the area of sky which have smaller angular distances. We therefore cannot rule out the possibility of these stars being extremely disturbed LMC disc stars. The other EE stars in the south-east have very different 3D velocities, reflecting the fact that towards the south, the LMC disc is kinematically disturbed (Cheng et al. 2022; Cullinane et al. 2022b).

In the south, stars from the LA group also show deviations from a disc in equilibrium. LA43 and LA44, previously identified as potential outliers based on their line-of-sight velocities and/or proper motions, have extreme V_ϕ velocities. LA43 is found to be counter-rotating with respect to the LMC disc, while moving inwards the LMC, with $V_\mathrm{R} \sim -50$ km s^{-1}. Stars from the LA group are located towards the same direction in which Olsen et al. (2011) found potential SMC debris, with apparent counter-rotating line-of-sight velocities. The CaT metallicity derived for LA43 is [Fe/H] $= -1.42$, in fair agreement with CaT metallicities for SMC stars. There are no spectroscopic studies in the literature with observations at angular distances > 18° in the southern area around the LMC, and therefore we cannot compare this result with previous observations.

The rest of the stars in the LA group are placed close to the southern arm-like feature reported in Belokurov & Erkal (2019). LA42 has 3D kinematics consistent with a disc in equilibrium, although the vertical distance is $\sim$8 kpc above the LMC disc plane. These results are in very good agreement with the measurements for field 26 from Cullinane et al. (2022b), which is very close to LA42 on the sky. LA40 and LA41 have negative inward velocities and positive out-of-plane velocities, consistent with perturbed disc material, in contrast to the relatively unperturbed inner southern LMC disc reported in Cullinane et al. (2022b), and in better agreement with the results from Cheng et al. (2022) for the southern periphery of the LMC.

7 COMPARISON WITH SIMULATIONS

7.1 Simulation setup

In order to explore how this dataset constrains the LMC-SMC interaction history, we produced a suite of numerical simulations. This suite is based on the simulations in Belokurov & Erkal (2019); Cullinane et al. (2022a, b). In particular, we model the interaction of the LMC-SMC in the presence of the Milky Way. We model the LMC with a Hernquist (Hernquist 1990) dark matter halo and an exponential stellar disc. For the Hernquist profile, we use a mass of $1.5 \times 10^{11} M_{\odot}$, motivated by the results of Erkal et al. (2019), and a scale radius of 20 kpc. This scale radius is chosen to match the circular velocity of the LMC measured at 8.7 kpc (van der Marel & Kallivayalil 2014). For the exponential disc, we use a mass of $2 \times 10^{9} M_{\odot}$, a scale radius of 1.5 kpc, and a scale height of 0.4 kpc. As in Cullinane et al. (2022a, b), we simulate the exponential disc with tracer particles and model the gravitational potential of the LMC with a particle sourcing the combined Hernquist and exponential disc potentials. We initialize the disc with 10^{7} particles using AGAMA (Vasiliev 2019) but only simulate the ~2500000 particles which have apocentres larger than 7 kpc since our dataset is focused on the outer LMC.

The potential of the SMC is modelled as a logarithmic sphere (i.e. with a flat rotation curve) within 2.9 kpc with a circular velocity of 60 km s^{-1}, based on the observations in Stanimirović, Staveley-Smith & Jones (2004). Beyond 2.9 kpc, the SMC is modelled as a Hernquist profile with a mass of $2.5 \times 10^{9} M_{\odot}$ and a scale radius of 0.043 kpc. This scale radius is chosen to match the observed circular velocity at 2.9 kpc. We note that we model the inner regions of the SMC as a logarithmic potential to avoid any unphysically large perturbations during its close encounter with the LMC disc. During the simulation, the SMC is modelled as a particle sourcing this potential.

The Milky Way is modelled as a 3-component system with an NFW dark matter halo, a Hernquist bulge, and a Miyammoto-Nagai disc based on the MWPOTENTIAL2014 model in Bovy (2015). The NFW halo has a mass of $8 \times 10^{11} M_{\odot}$, a scale radius of 16 kpc, and a concentration of 15.3. The Miyamoto-Nagai disc has a mass of $6.8 \times 10^{10} M_{\odot}$, a scale radius of 3 kpc, and a scale height of 0.28 kpc. The Hernquist bulge has a mass of $5 \times 10^{9} M_{\odot}$ and a scale radius of 0.5 kpc. During the simulation, the Milky Way is allowed to move in response to the LMC and SMC. This is done by treating the Milky Way as a single particle which sources its three-component potential.

During each simulation, the LMC and SMC are initialized given their present-day position and velocity with the Milky Way placed at the origin. The Milky Way, LMC, and SMC are rewound for 2 Gyr. At this time, the tracer particles representing the LMC disc are injected and the simulation is evolved to the present day. Since the tracer particles have a range of orbital timescales with respect to the LMC, the tracer particles are individually evolved to the present day for computational efficiency. We emphasize that these are not full *N*-body simulations (e.g. as in Besla et al. 2012) and thus they do not capture the self-gravity effects of the perturbed LMC disc or the deformation of the LMC in response to the Milky Way (e.g. Garavito-Camargo et al. 2019). However, they are useful for exploring a large range of SMC-LMC encounters in a computationally efficient manner. A detailed discussion of the caveats of these models can be found in section 4.3.1 of Cullinane et al. (2022a).

Our suite consists of four sets of 100 simulations of the LMC-SMC-Milky Way encounter which differ in the present-day LMC and SMC positions and velocities. For the first set, we sampled the LMC and SMC position and velocity based on observations of their proper motions, radial velocities, and distances from van der Marel et al. (2002), Harris & Zaritsky (2006), Kallivayalil et al. (2013), Graczyk et al. (2014), and Pietrzyński et al. (2019), respectively. We then simulated 100 realizations of the LMC and SMC's present-day positions and velocities and simulated each of these. Interestingly, in 51 of these realizations, the SMC has a negligible effect on the LMC disc since it has no close crossings with the LMC disc in the past, and thus the majority of the simulations in this suite were essentially unperturbed. For the second suite of 100 simulations, we again sampled from the LMC and SMC's present-day positions and velocities. However, for each sample, we then integrated the LMC-SMC-Milky Way orbit for 2 Gyr and required that there was at least one LMC disc crossing more ancient than 250 Myr ago.

For the third set of simulations in the suite, we explored a slightly larger range of LMC–SMC interactions by considering larger errors on the present-day position and velocity of the LMC and SMC. This was done by accounting for the systematic uncertainty on the LMC and SMC proper motions and by accounting for the uncertainty in the on-sky location of the SMC and LMC. For the LMC, we used proper motions of $(\mu_{\alpha}^{*}, \mu_{\delta}) = (-1.865 \pm 0.015, 0.331 \pm 0.049)$ mas yr^{-1} and $(\alpha, \delta) = (80\overset{\circ}{.}440 \pm 0\overset{\circ}{.}725, -69\overset{\circ}{.}238 \pm 0\overset{\circ}{.}243)$. The proper motions come from Gaussian fits to the proper motion measurements in Kallivayalil et al. (2013), Wan et al. (2020), Gaia Collaboration (2021), Choi et al. (2022), and Niederhofer et al. (2022). The on-sky location comes from a Gaussian fit to the centres measured in van der Marel et al. (2002), van der Marel & Kallivayalil (2014), Wan et al. (2020), Gaia Collaboration (2021), Choi et al. (2022), and Niederhofer et al. (2022). For the SMC we used a proper motion of $(\mu_{\alpha}^{*}, \mu_{\delta}) = (-0.734 \pm 0.017, -1.227 \pm 0.010)$ mas yr^{-1} and $(\alpha, \delta) = (14.^{\circ}255 \pm 1.^{\circ}713, -71.^{\circ}710 \pm 0.^{\circ}338)$. For the proper motions we use Gaussian fits to the proper motion measurements in Kallivayalil et al. (2013); De Leo et al. (2020); Niederhofer et al. (2021). For the on-sky location we use Gaussian fits to the measurements in de Vaucouleurs & Freeman (1972); Kallivayalil et al. (2013); Ripepi et al. (2017); Di Teodoro et al. (2019). As with the second set in the suite, we required that each of the 100 realizations had at least one SMC-LMC disc crossing more ancient than 250 Myr ago.

For the final suite of 100 simulations, we found a particular realization which was a good match to the data (see Section 7.2) and simulated 100 realizations with similar phase-space coordinates for the LMC and SMC. This was done by using k-Nearest Neighbours (with $k = 5$) to estimate the covariance matrix for the LMC-SMC observables. The 100 realizations were drawn from this covariance matrix. This final set of 100 simulations all had at least one LMC disc crossing more ancient than 250 Myr.

7.2 Comparison with observations

In order to compare the 6D phase-space of the model kinematics with our observations, all particles within a two-degree radius around each (R.A., Dec.) position were selected. This radius was chosen to retrieve at least ten model particles even in the case of the stars at larger distances from the LMC (i.e. those more than 15° from the LMC centre). We estimated the median proper motion, line-of-sight velocity and heliocentric distance of the model particles inside this radius around each of our target stars, in each of the model realizations. Then, a log-likelihood was estimated for each of the model realizations, as

$$\log \mathcal{L} = \sum_{i,j} -\frac{1}{2} \log \left(2\pi \sigma_{i,j}^{2}\right) - \frac{1}{2} \frac{(m_{i,j,\mathrm{data}} - m_{i,j,\mathrm{model}})^{2}}{\sigma_{i,j}^{2}}, \qquad (5)$$

where i are the observed values for the individual stars and the corresponding values for the particles in the simulations, and j the four dimensions ($\mu_{\alpha *}$, μ_{δ}, V_{rad}, Distance). The dispersion $\sigma_{\mathrm{i,j}}$ corresponds to the sum in quadrature of the standard deviation of

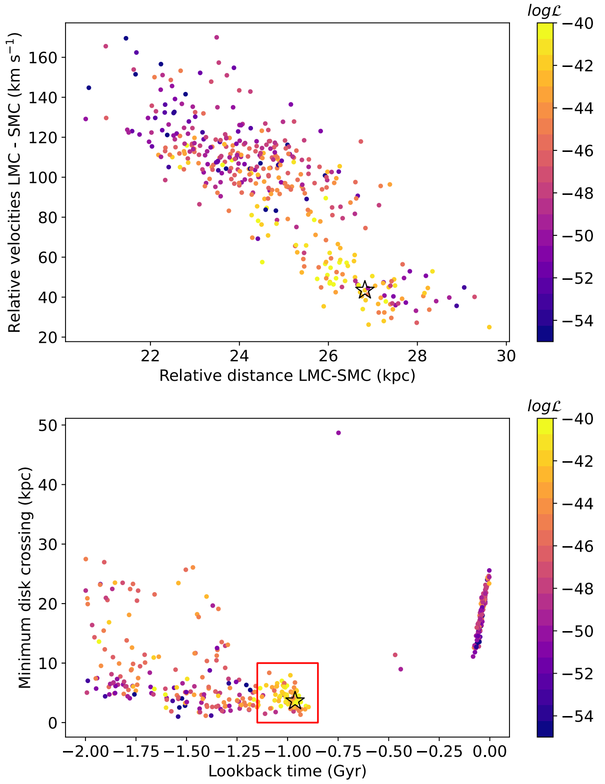

Figure 16. Top panel: present-day relative distance and velocity between the LMC and SMC in the numerical simulations. Each simulation is colour-coded according to the log-likelihood (as described in the text). Bottom panel: lookback time and the minimum radial distance r of the SMC at the time it crosses the LMC's disc. The red box marks those simulations with the largest log-likelihood, i.e. those that are a better representation of our observations.

each component and the errors for proper motions, radial velocities and distances.

In the top panel of Fig. 16, the present-day relative 3D position and velocities of the LMC and SMC, for each of the 400 model realizations, are shown, colour-coded by the log-likelihood. Those in which the present-day relative distance between the Clouds is between 25 and 27 kpc, with relative velocities between 80 and 30 km s^{-1} have the largest $\log \mathcal{L}$, i.e. they best resemble the observations. The model realization that motivates the fourth suite of simulations discussed above is marked with a black star in both panels. For this comparison, the potential kinematic outliers (see Section 6) were not included. If they are, the results do not change significantly, and only the values for the log-likelihood decrease as the simulations are not able to reproduce the data, particularly for those stars with extreme kinematics.

Each of the model realizations has a different interaction history between the Clouds. In particular, the SMC crosses the LMC disc between one to six times in the last 2 Gyr. The bottom panel of Fig. 16 shows the lookback time for the closest approach of the SMC to the LMC versus the radial crossing distance. Based on the log-likelihood, the simulations in which the SMC crossed the LMC's disc plane between ∼1.15 and 0.85 Gyr ago, with the SMC at a radial crossing distance $r \lesssim 10$ kpc from the LMC have higher log-likelihood values, although there is no perfect match between any of the model realizations and our observations.

Fig. 17 shows the spatial density (left-hand panel), the median in-plane radial velocity V_R (middle panel) and out-of-plane vertical velocity V_Z (right-hand panel) for one of the model realizations with the largest $\log \mathcal{L}$, and the corresponding positions and observed velocities for each of our targets. The left panel includes the locations of the SMC during the three LMC's disc crossing in this particular realization, at 360 Myr ago, 1.0 and 1.9 Gyr ago. A reasonable agreement, with a similar order of magnitude as those observed, is found for the in-plane radial velocities, while the vertical motions have larger discrepancies. The fact that there is no single model realization that is able to completely reproduce our 6D phase-space observations reflects the complex parameter space and interaction history of the past orbits of the Clouds.

Based on the radial velocities, the simulation is able to reproduce the inward motion of the MS stars and those stars in the LA group (southern outer disc). In the case of the stars on the eastern side, the northern EE stars ($\eta > 0°$) have outwards in-plane radial motions, possibly due to being pulled out from the LMC at a different time than the stars in the north or south. South-eastern stars present both inward and outward motions, which could be explained as the result of the successive SMC's disc crossings.

The vertical velocities of the MS stars are almost zero, given their locations in the LMC disc plane, while the potential outlier, MS02, has a larger positive vertical velocity. While in the case of EE stars, the vertical motion is less coherent, some stars having positive and others negative in-plane velocities. LA stars have out-of-equilibrium V_z velocities, similar to the median values found in this particular model realization.

Overall, this picture in which at least two SMC's disc crossings, besides the most recent one at ∼150 Myr ago, is consistent with the analysis in Cullinane et al. (2022b). In that work, the Clouds orbits were traced back up to 1 Gyr ago, and older interactions were not explored. In this work, the orbits are traced up to 2 Gyr back and even though most of the model realizations have a disc crossing more than 1.3 Gyr ago, the radial crossing distance is generally much larger than $\simeq$10 kpc. There is a small number of model realizations in which the disc crossing at ∼ 2 Gyr has the smallest radial crossing distance (i.e. the one that most affected the LMC disc) along the past SMC orbit. Fig. 16 shows that many but not all of them have a relatively large log-likelihood, and therefore the impact of an older disc crossing as the most important perturbation of the LMC disc cannot be fully ruled out.

Among those model realizations inside the red box in Fig. 16, which have high log-likelihood, we investigated the individual orbits of the SMC around the LMC. We found that all of those model realizations have the SMC crossing the LMC's disc three times, at 1.8 ± 0.1 Gyr ago, 989 ± 44 Myr ago, and at ∼320 ± 26 Myr ago. During these three times, the SMC crossed the disc of the LMC at radial crossing distances of 5.6 ± 1.7 kpc, 4.4 ± 1.3 kpc, and 10.0 ± 2.3 kpc, respectively. The reported values are the mean and standard deviation values based on the individual values for the 40 model realizations inside the red box in Fig. 16, having $\log \mathcal{L}$ up to 3.0 dex below the maximum $\log \mathcal{L}$ value. The standard deviations of the impact parameters are relatively low, reflecting that the past interaction histories of this subsample of model realizations are very similar. Based on these mean values, the radial crossing distances at ∼1.8 Gyr and ∼950 Myr ago are very similar, and consistent with two close pericentric passages of the SMC. The mean pericentric radial and vertical distances in this subsample of model realizations are $r_{\rm peri} = 5.3 \pm 1.3$ kpc, $z_{\rm peri} = 4.7 \pm 1.2$ kpc (at ∼260 Myr ago), $r_{\rm peri} = 4.3 \pm 1.3$ kpc, $z_{\rm peri} = -0.8 \pm 0.7$ kpc (at ∼980 Myr ago), and $r_{\rm peri} = 4.5 \pm 1.0$ kpc, $z_{\rm peri} = -2.3 \pm 1.1$ kpc (at ∼1.81 Gyr ago). The most

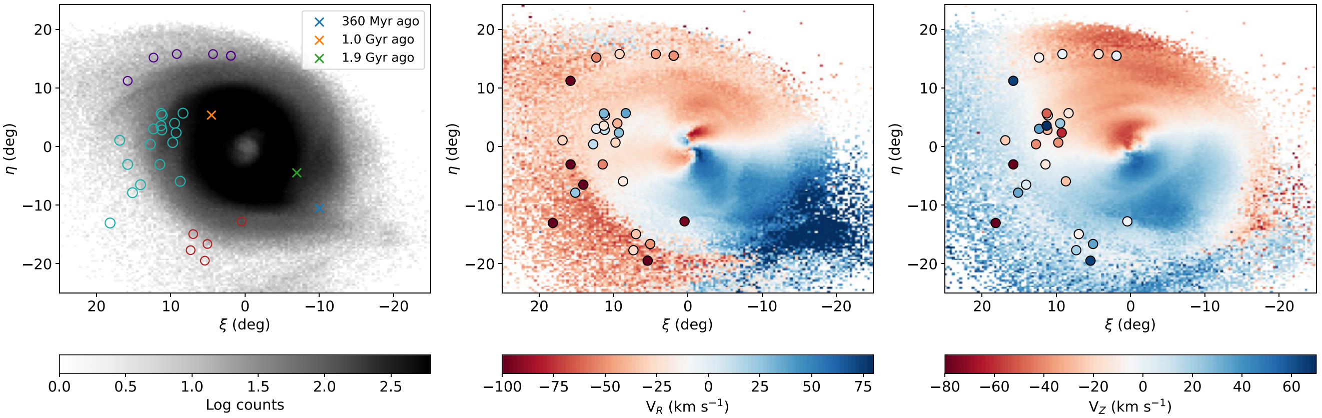

Figure 17. Left panel: spatial density of the particles in one of the model realizations with the largest log-likelihood. The position of our targets and the original location of the three disc crossings are shown. Middle and right panels: in-plane and out-of-plane median velocities for the particles in the same model realization. The individual points are all the Mira-like stars in the vicinity of the Clouds, including those potential outliers (marked with open squares in Fig. 13).

recent pericentric passage is consistent with previous studies (Choi et al. 2022; Cullinane et al. 2022b) in time and pericentric distance, while the vertical distance at pericentre is similar to the values reported in Cullinane et al. (2022b)[5] In both previous encounters, the pericentric distance of the SMC is on the order of ∼4.5 kpc, closer than the most recent interaction.

8 SUMMARY AND CONCLUSIONS

We have carried out a spectroscopic follow-up for more than 40 Mira candidates around the LMC. Radial velocities obtained from low-resolution spectra, as well as stellar parameters, were derived for all the targets. Using *Gaia* DR3 parallaxes, foreground stars among our sample were discarded.

For a subsample of the remaining stars, light curves and pulsation periods were found, confirming their variable nature. After classifying the stars as C-/O-rich based on the Wesenheit function $W_{J,\,K_s}$, the most likely pulsation mode was assigned based on the known distribution of LPVs around the LMC. Heliocentric distances based on PL relations were estimated for those stars with periods in the literature. We compared the distances obtained in this way with the median distance of RRL stars around each of the Mira candidates, finding a reasonable agreement. We therefore adopted the RRL-based distance for the complete sample. The 6D phase-space information was obtained for 27 Mira candidates, finding that most of them have kinematics and metallicities consistent with being perturbed LMC disc population. For the subgroup of 14 stars located above the Galactic plane, we were not able to estimate a reliable heliocentric distance, although based on their proper motions these stars are most likely distant Galactic Miras.

A suite of numerical simulations for the LMC/SMC past interaction history (including the Milky Way) was run. From the phase-space properties of the simulated particles, the most likely simulations given our observations were identified. A scenario in which the SMC has had three close pericentric passages around the LMC seems to best resemble our observations. This particular interaction history is characterized by three LMC disc crossings of the SMC. The oldest occurred at ∼1.78 Gyr (impact parameter of 5.6 kpc), which is similar to the time at which a peak in the star formation history (SFH) of the LMC has been found (Ruiz-Lara et al. 2020), and the expected time for the formation of the gaseous Leading Arm (Besla et al. 2010; Diaz & Bekki 2012). After this, a second disc crossing took place at ∼950 Myr ago (disc crossing distance of ∼4.4 kpc), with this event the one that most significantly impacted the LMC periphery. A most recent disc crossing, only ∼350 Myr ago (disc crossing distance of ∼10.0 kpc) was also found to be required to recover similar kinematics to our observations. The timing of these three disc crossings is in good agreement with the times at which enhancement in the SFH of the Clouds has been recently reported in Massana et al. (2022). In that work, a synchronized enhancement of the SFH of both Clouds is found at ∼ 0.45 Gyr, ∼1 and ∼ 2 Gyr ago, which are interpreted as the result of close encounters.

In summary, our observations and their comparison with the numerical simulations provide a useful constraint on the past interaction history of the Clouds, in which at least three close interactions have happened, highly disturbing the motions of the stars in the LMC periphery. Our results are similar to previous studies that claimed one or two disc crossings in the last 1 Gyr, with this work studying more distant stars (relative to the LMC centre), and performing a longer integration of the Clouds' orbit (up to 2 Gyr ago). This old time of SMC disc crossing has a radial crossing distance of only 5.0 kpc, similar to the radial crossing distance for the interaction occurred at 980 Myr. These two events are therefore the ones that most significantly perturbed the LMC disc stars. Future spectroscopic campaigns of the complete Magellanic periphery are crucial to obtain robust measurements of the stellar kinematics at different angular separations and position angles around the Clouds.

ACKNOWLEDGEMENTS

Based on observations made at Cerro Tololo Inter-American Observatory at NSF's NOIRLab (NOIRLab Prop. ID: 2017B-0910; PI: M. Catelan), which is managed by the Association of Universities for Research in Astronomy (AURA) under a cooperative agreement with the National Science Foundation. This work has made use of data from the European Space Agency (ESA) mission *Gaia* (https://www.cosmos.esa.int/gaia), processed by the *Gaia* Data Processing and Analysis Consortium (DPAC, https://www.cosmos.esa.int/web/gaia/dpac/consortium). Funding for the DPAC has been provided by

---

[5] The sign convention for the z-axis in this work is the opposite of the one adopted in Cullinane et al. (2022b).

national institutions, in particular the institutions participating in the *Gaia* Multilateral Agreement.

JAC-B acknowledges support from FONDECYT Regular N1220083. DA acknowledges support from the European Research Council (ERC) Starting Grant NEFERTITI H2020/808240. DA also acknowledges financial support from the Spanish Ministry of Science and Innovation (MICINN) under the 2021 Ramón y Cajal program MICINN RYC2021-032609.

DATA AVAILABILITY

All the data reduced and analysed for this paper are fully available on reasonable request to the corresponding authors.[6]

REFERENCES

Allende Prieto C., Beers T. C., Wilhelm R., Newberg H. J., Rockosi C. M., Yanny B., Lee Y. S., 2006, ApJ, 636, 804

Allende Prieto C., Koesterke L., Hubeny I., Bautista M. A., Barklem P. S., Nahar S. N., 2018, A&A, 618, A25

Andrae R. et al., 2022, preprint (arXiv:2206.06138)

Belokurov V. A., Erkal D., 2019, MNRAS, 482, L9

Belokurov V., Erkal D., Deason A. J., Koposov S. E., De Angeli F., Evans D. W., Fraternali F., Mackey D., 2017, MNRAS, 466, 4711

Besla G., Kallivayalil N., Hernquist L., van der Marel R. P., Cox T. J., Kereš D., 2010, ApJ, 721, L97

Besla G., Kallivayalil N., Hernquist L., van der Marel R. P., Cox T. J., Kereš D., 2012, MNRAS, 421, 2109

Bovy J., 2015, ApJS, 216, 29

Castelaz M. W., Luttermoser D. G., Caton D. B., Piontek R. A., 2000, AJ, 120, 2627

Cheng X. et al., 2022, ApJ, 928, 95

Choi Y. et al., 2018, ApJ, 866, 90

Choi Y., Olsen K. A. G., Besla G., van der Marel R. P., Zivick P., Kallivayalil N., Nidever D. L., 2022, ApJ, 927, 153

Cullinane L. R. et al., 2020, MNRAS, 497, 3055

Cullinane L. R., Mackey A. D., Da Costa G. S., Erkal D., Koposov S. E., Belokurov V., 2022a, MNRAS, 510, 445

Cullinane L. R., Mackey A. D., Da Costa G. S., Erkal D., Koposov S. E., Belokurov V., 2022b, MNRAS, 512, 4798

Cullinane L. R., Mackey A. D., Da Costa G. S., Koposov S. E., Erkal D., 2023, MNRAS, 518, L25

Deason A. J., Belokurov V., Koposov S. E., Gómez F. A., Grand R. J., Marinacci F., Pakmor R., 2017, MNRAS, 470, 1259

De Leo M., Carrera R., Noël N. E. D., Read J. I., Erkal D., Gallart C., 2020, MNRAS, 495, 98

de Vaucouleurs G., Freeman K. C., 1972, Vistas in Astronomy, 14, 163

Diaz J. D., Bekki K., 2012, ApJ, 750, 36

Di Teodoro E. M. et al., 2019, MNRAS, 483, 392

Drake A. J. et al., 2017, MNRAS, 469, 3688

El Youssoufi D. et al., 2021, MNRAS, 505, 2020

Erkal D. et al., 2019, MNRAS, 487, 2685

Gaia Collaboration, 2021, A&A, 649, A7

Gaia Collaboration, 2023, A&A, in press

Garavito-Camargo N., Besla G., Laporte C. F. P., Johnston K. V., Gómez F. A., Watkins L. L., 2019, ApJ, 884, 51

Gatto M., Ripepi V., Bellazzini M., Tortora C., Tosi M., Cignoni M., Longo G., 2022, ApJ, 931, 19

Gillet D., Ferlet R., Maurice E., Bouchet P., 1985, A&A, 150, 89

Graczyk D. et al., 2014, ApJ, 780, 59

Grady J., Belokurov V., Evans N. W., 2021, ApJ, 909, 150

Harris J., Zaritsky D., 2006, AJ, 131, 2514

Hernquist L., 1990, ApJ, 356, 359

Jayasinghe T. et al., 2018, MNRAS, 477, 3145

Jiménez-Arranz Ó. et al., 2023, A&A, 669, A91

Joy A. H., 1926, ApJ, 63, 281

Kallivayalil N., van der Marel R. P., Besla G., Anderson J., Alcock C., 2013, ApJ, 764, 161

Katz D. et al., 2023, A&A, in press

Koesterke L., Allende Prieto C., Lambert D. L., 2008, ApJ, 680, 764

Lebzelter T., Mowlavi N., Marigo P., Pastorelli G., Trabucchi M., Wood P. R., Lecoeur-Taïbi I., 2018, A&A, 616, L13

Lebzelter T., Trabucchi M., Mowlavi N., Wood P. R., Marigo P., Pastorelli G., Lecoeur-Taïbi I., 2019, A&A, 631, A24

Mackey A. D., Koposov S. E., Erkal D., Belokurov V., Da Costa G. S., Gómez F. A., 2016, MNRAS, 459, 239

Mackey D., Koposov S., Da Costa G., Belokurov V., Erkal D., Kuzma P., 2018, ApJ, 858, L21

Martini P. et al., 2014, in Ramsay S. K., McLean I. S., Takami H.eds, Proc. SPIE Conf. Ser. Vol. 9147, Ground-based and Airborne Instrumentation for Astronomy V. SPIE, Bellingham, p. 91470Z

Massana P. et al., 2022, MNRAS, 513, L40

Menzies J. W., Feast M. W., Whitelock P. A., 2006, MNRAS, 369, 783

Niederhofer F. et al., 2021, MNRAS, 502, 2859

Niederhofer F. et al., 2022, MNRAS, 512, 5423

Olsen K. A. G., Salyk C., 2002, AJ, 124, 2045

Olsen K. A. G., Zaritsky D., Blum R. D., Boyer M. L., Gordon K. D., 2011, ApJ, 737, 29

Petersen M. S., Peñarrubia J., Jones E., 2022, MNRAS, 514, 1266

Pietrzyński G. et al., 2019, Nature, 567, 200

Ripepi V. et al., 2017, MNRAS, 472, 808

Ruiz-Lara T. et al., 2020, A&A, 639, L3

Santana F. A. et al., 2021, AJ, 162, 303

Skrutskie M. F. et al., 2006, AJ, 131, 1163

Soszynski I. et al., 2007, AcA, 57, 201

Stanimirović S., Staveley-Smith L., Jones P. A., 2004, ApJ, 604, 176

Tody D., 1993, in Hanisch R. J., Brissenden R. J. V., Barnes J.eds, ASP Conf. Ser. Vol. 52, Astronomical Data Analysis Software and Systems II. Astron. Soc. Pac., San Francisco, p. 173

Tonry J., Davis M., 1979, AJ, 84, 1511

van der Marel R. P., Cioni M.-R. L., 2001, AJ, 122, 1807

van der Marel R. P., Kallivayalil N., 2014, ApJ, 781, 121

van der Marel R. P., Alves D. R., Hardy E., Suntzeff N. B., 2002, AJ, 124, 2639

Vasiliev E., 2019, MNRAS, 482, 1525

Wan Z., Guglielmo M., Lewis G. F., Mackey D., Ibata R. A., 2020, MNRAS, 492, 782

Wright E. L. et al., 2010, AJ, 140, 1868

Zhao H., Evans N. W., 2000, ApJ, 545, L35

APPENDIX A: GAIA DR3 PARAMETERS

Table A1 includes the *Gaia* source ID, parallax, stellar parameters (T_{eff}, log$g$, [Fe/H]), and spectral type, if available, for our targets.

---

[6] david.aguado@unifi.it, camila.navarrete@oca.eu

Table A1. *Gaia* DR3 stellar parameters for our targets. The effective temperature, surface gravity, and metallicity reported are those derived from the GSP-Phot Aeneas best library using BP/RP spectra and correspond to the table columns `teff_gspphot, logg_gspphot, mh_gspphot`, respectively, from the `gaiadr3.gaia_source` table. The spectral type corresponds to the column `spectraltype_esphs` from the `gaiadr3.astrophysical_parameters` table.

ID	Source ID	Parallax (mas)	T_{eff} (K)	logg (cm s^{-2})	[Fe/H]	SpType
BP22	5460206736750537856	0.0323	4301.4	1.8898	0.1705	K
BP23	3459149244108017408	0.0291				M
BP24	5397474650583084160	–0.0207				M
BP25	5447608326360545792	–0.0371				M
BP26	5442937635326305920	0.0011	4818.8	2.0640	–0.5251	M
BP27	5449164032234750720	0.0089				M
BP28	5672923478937609088	0.0155	33327.2	4.0456	0.0024	K
BP29	5376950032669120768	3.2880				M
BP30	3557444548542598912	3.1706				M
BP31	3571469235968627840	2.0531	3639.7	4.0367	–1.0212	M
BP32	5677088493408045568	0.0070				K
BP33	5670783966749167616	0.0361	4807.5	2.0942	–0.5508	M
BP34	3556135034489468672	2.9397	3724.6	4.5989	–0.3160	M
BP35	3483101245925708032	0.0134				K
BP36	5379917099154530944	0.0287	3410.1	0.0619	–0.4300	M
BP37	3458916766118414592	0.0249	4406.8	2.0834	0.7920	K
BP38	3477205424060762112	0.0086	4258.6	2.0246	0.2059	M
BP39	3484343968942530304	0.0027				M
EE06	5222307398713735296	–0.0231	4404.8	2.1391	0.1030	K
EE07	5273716228803929088	–0.0014				M
EE08	5287270909369746176	–0.0161	4422.5	2.6345	0.1550	K
EE09	5282142924576162816	–0.0360	4623.9	2.8845	0.3508	K
EE10	5262926244460395520	0.0073				M
EE11	5281337704108065280	0.0270	4335.3	1.8110	0.2600	K
EE12	5282659076566187776	0.0211	4503.9	2.6225	0.1709	K
EE13	5288705943842258304	0.0045	4347.6	1.8085	0.2000	K
EE14	5285751693536837376	–0.0171				
EE15	5286801074305659520	0.0301	4670.9	2.7438	0.1568	K
EE16	5285520967893476224	–0.0178				CSTAR
EE17	5221807017844430592	–0.0182				M
EE18	5272890568589181952	–0.0102	4436.3	2.2757	0.1279	K
EE19	5478725879815547520	–0.0342	4546.5	2.5079	0.4875	K
EE20	5277501920355575808	0.0105	4500.4	2.6607	0.2807	K
EE21	5287009569198354816	–0.0173				M
EE22	5242317166011623808	0.0342				K
LA40	5192498745130957824	–0.0381	4327.7	2.0829	0.1371	K
LA41	5194991505491879168	–0.0063				K
LA42	5196276426565456128	–0.0170				M
LA43	5191672668300504832	–0.0044	4902.0	2.1046	–1.2015	M
LA44	4621336230122857216	–0.0028	5018.7	2.5114	–0.7710	M
MS01	4791851791893295104	–0.0500				M
MS02	5490523880100951552	–0.0229				K
MS03	5498652260326236288	–0.0514	4382.8	2.3396	0.7982	K
MS04	4768385293178232064	–0.0176	4536.1	1.7935	–0.5526	M
MS05	5499999780546395520	–0.0473				K

This paper has been typeset from a TEX/LATEX file prepared by the author.

Published by Oxford University Press on behalf of Royal Astronomical Society